MDPI

Article

Evaluating the Two-Source Energy Balance Model Using MODIS Data for Estimating Evapotranspiration Time Series on a Regional Scale

Mahsa Bozorgi [1,2,*], Jordi Cristóbal [1] and Magí Pàmies-Sans [2]

1   Department of Geography, Universitat Autònoma de Barcelona, Campus de Bellaterra, Edifici B, Carrer de la Fortuna, s/n, 08193 Bellaterra, Spain; jordi.cristobal@uab.cat
2   Efficient Use of Water in Agriculture Program, Institute of Agrifood Research and Technology, Fruitcentre, Parc Científic i Tecnològic Agroalimentari de Lleida 23, 25003 Lleida, Spain; magi.pamies@irta.cat
*   Correspondence: mahsa.bozorgi@irta.cat

Abstract: Estimating daily continuous evapotranspiration (ET) can significantly enhance the monitoring of crop stress and drought on regional scales, as well as benefit the design of agricultural drought early warning systems. However, there is a need to verify the models' performance in estimating the spatiotemporal continuity of long-term daily evapotranspiration (ET_d) on regional scales due to uncertainties in satellite measurements. In this study, a thermal-based two-surface energy balance (TSEB) model was used concurrently with Terra/Aqua MODIS data and the ERA5 atmospheric reanalysis dataset to calculate the surface energy balance of the soil–canopy–atmosphere continuum and estimate ET at a 1 km spatial resolution from 2000 to 2022. The performance of the model was evaluated using 11 eddy covariance flux towers in various land cover types (i.e., savannas, woody savannas, croplands, evergreen broadleaf forests, and open shrublands), correcting for the energy balance closure (EBC). The Bowen ratio (BR) and residual (RES) methods were used for enforcing the EBC in the EC observations. The modeled ET was evaluated against unclosed ET and closed ET (ET_{BR} and ET_{RES}) under clear-sky and all-sky observations as well as gap-filled data. The results showed that the modeled ET presented a better agreement with closed ET compared to unclosed ET in both Terra and Aqua datasets. Additionally, although the model overestimated ET_d across all different land cover types, it successfully captured the spatiotemporal variability in ET. After the gap-filling, the total number of days compared with flux measurements increased substantially, from 13,761 to 19,265 for Terra and from 13,329 to 19,265 for Aqua. The overall mean results including clear-sky and all-sky observations as well as gap-filled data with the Aqua dataset showed the lowest errors with ET_{RES}, by a mean bias error (MBE) of 0.96 mm.day^{-1}, an average mean root square (RMSE) of 1.47 mm.day^{-1}, and a correlation (r) value of 0.51. The equivalent figures for Terra were about 1.06 mm.day^{-1}, 1.60 mm.day^{-1}, and 0.52. Additionally, the result from the gap-filling model indicated small changes compared with the all-sky observations, which demonstrated that the modeling framework remained robust, even with the expanded days. Hence, the presented modeling framework can serve as a pathway for estimating daily remote sensing-based ET on regional scales. Furthermore, in terms of temporal trends, the intra-annual and inter-annual variability in ET can be used as indicators for monitoring crop stress and drought.

Keywords: remote sensing-based evapotranspiration; two-source energy balance; MODIS; drought

1. Introduction

According to the Intergovernmental Panel on Climate Change Assessment Report (IPCC), European Mediterranean areas have experienced an increase in the frequency of concurrent droughts and heatwaves since the 1950s [1], associated with rising extreme temperatures and decreasing precipitation [2]. The Mediterranean climate is characterized by water-limited crop production; therefore, mapping the long-term spatiotemporal variability

in evapotranspiration (ET) is critical for comprehensively understanding how ecosystems respond to climate changes.

ET plays a critical role in the climate system by exchanging energy and mass between the land surface and atmosphere, which sequentially affects plant growth and yield [3–5]. The estimation of daily evapotranspiration (ET_d) is critical for achieving efficient water use in irrigated agricultural areas [6] by determining crop water requirements [7], scheduling irrigation, and optimizing water use, especially in water-limited regions [8]. Additionally, the spatiotemporal variability in ET_d can reflect ecosystem responses to hazards such as droughts [9] and climate changes [10], aiding in the design of early warning systems [11].

ET can be estimated with ground-based and remote sensing-based observations. Conventional ground observation methods, including lysimeters [12], the Bowen ratio [13], and eddy covariance systems [14], rely on direct ground measurements. Although these point-scale measurements have shown relatively accurate ET measurements for homogeneous areas, they have a limited ability to quantify the spatial variability in ET on regional scales due to spatial heterogeneity. Remote sensing data have revolutionized water resource management by providing continuous spatial and temporal information, even from remote and inaccessible regions, at various resolutions, which can address the limitations of ground observations [15–18].

There are various methods for estimating ET using remotely sensed land surface temperature (LST) [19]. Thermal-based surface energy balance (SEB) models are widely used to map ET by estimating surface energy fluxes [20–24]. SEB models consider the latent heat flux (LE), which represents the energy used for soil evaporation and plant canopy transpiration, as the differences between available energy (i.e., net radiation (R_n) and soil heat flux (G)) and sensible heat flux (H) [25]. However, there are challenges associated with satellite retrievals of LST [26]. Remote sensing-based LST integrates thermal data from both soil and vegetation components. Dual-source models have been introduced to overcome this limitation by petitioning radiometric temperature between soil and vegetation. These models differentiate soil and vegetation energy fluxes when estimating H and LE, showing better performance on vegetation–soil-mixed surfaces compared to signal-source models that assume the land surface as a signal system [27]. An example of a dual-source model is the TSEB model developed by [28,29], which has been successfully applied in various environments and land covers worldwide. The TSEB model minimizes uncertainties related to user experience, similar to the Surface Energy Balance Algorithm for Land (SEBAL) [30] and Mapping Evapotranspiration at high Resolution with Internalized Calibration (METRIC) [31]. When comparing SEBAL with TSEB, [32] found that TSEB outperformed SEBAL in areas with bare soil and sparse vegetation. Modifications to SEBAL inputs improved accuracy for specific land cover types but exacerbated discrepancies for others, further highlighting the model's limitations [32]. Additionally, [33] found that TSEB performed better compared to METRIC in estimating instantaneous ET.

However, the accuracy of the TSEB model is determined by the quality of the input data. Moreover, the parameterization of vegetation in flux estimation is one of the challenges in the application of the TSEB model, which can significantly influence the outputs [34,35]. The Atmosphere–Land Exchange Inverse (ALEXI) model introduced by [36] applied TSEB at two times to improve soil and vegetation components. The ALEXI disaggregation (DisALEXI) approach [33] aimed to improve the spatial resolution of the coarse temporal scale of the ALEXI model. The SEN-ET modeling framework "https://www.esa-sen4et.org (accessed on 19 March 2023)" [37] is another recent development, with significant improvements in the implementation of the TSEB model using the European Union's Copernicus Earth Observation data (Sentinel-3 and -2) and meteorological reanalysis from ERA5 to estimate land surface fluxes, including ET_d, at a 20 m resolution.

Numerous ET products have been developed based on remote sensing observations, SEB models, and machine learning, each offering different spatial and temporal resolutions [38]. Daily ET products such as GLEAM [39] and SSEBop [40] are available, at coarse spatial resolutions. However, finer-scale ET mapping is required to enhance water re-

source management and drought monitoring [7]. Conversely, products like MOD16 [41], GLASS [42], and BESS provide high spatial resolution (1 km) but only at 8-day intervals, limiting their ability to monitor the sub-seasonal (weekly) variability in ET.

Consequently, although numerous ET products are available on multiple spatial and temporal scales, there is still a lack of spatiotemporal continuous estimation of long-term ET_d at a 1 km spatial resolution across southern Europe. Furthermore, many published studies only evaluated the performance of ET models over the crop growth period of a single year or short periods [24,43]. However, ET estimation approaches should be capable of capturing ET spatiotemporal year-round variability.

Hence, this study aims to address these gaps by (1) estimating the ET_d time series at two satellite overpasses using Terra and Aqua MODIS images at a 1 km spatial resolution from 2000 to 2022, and (2) comparing the performance of the TSEB model with long-term ground-based measurements under various land covers and environmental conditions to evaluate year-round model performance.

2. Materials and Methods

2.1. Study Area

The study area covers the entire of the Iberina Peninsula (IP) and the southern part of France, including regions with both Mediterranean and coastal climates. This area is among the most vulnerable regions in southern Europe due to its heterogeneous atmospheric influences [44], Mediterranean climate, and agricultural predominance [45]. The diverse atmospheric patterns in this area lead to significant variability in precipitation, contributing to recurrent droughts and a notable trend toward increasing dryness over the last few decades [46–48]. Figure 1 shows the study area, and the 11 selected flux towers used to evaluate the model.
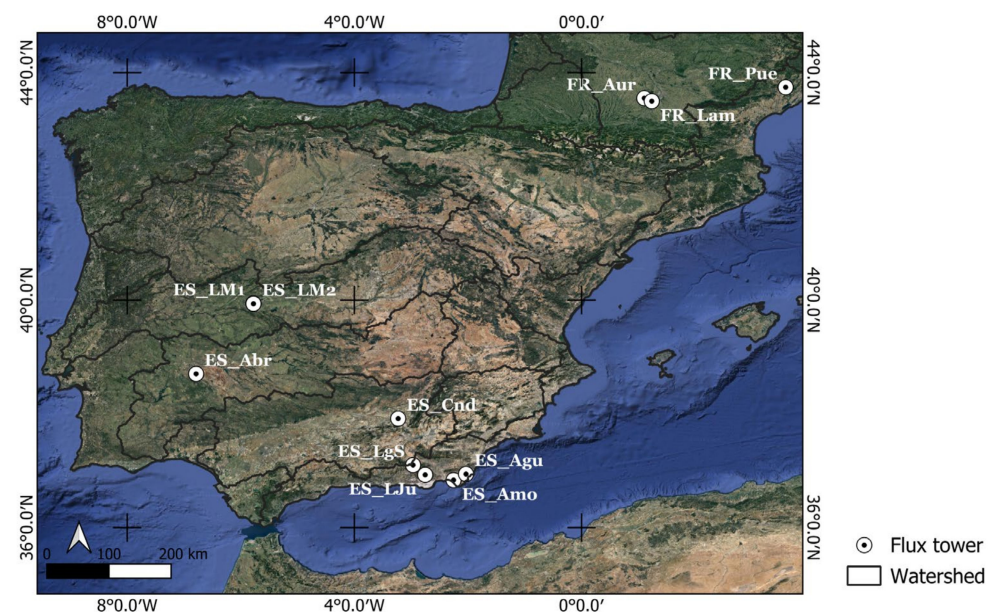

Figure 1. Location of the study area and the 11 selected flux towers. Projection system in UTM-30N WGS-84.

2.2. Data

2.2.1. Remote Sensing and Reanalysis Dataset TSEB Inputs

The remote sensing and climate reanalysis data (ERA5) used to implement the TSEB model in this study are described in Table 1.

Table 1. The input data used in the TSEB model.

Data	Products	Variables	Resolution	
			Temporal	**Spatial**
MODIS/Terra	MOD09G	Surface reflectance, NDVI	Daily	500 m
	MOD11A1	LST, emissivity	Daily	1000 m
MODIS/Aqua	MYOD09	Surface reflectance, NDVI	Daily	500 m
	MYD11A1	LST, emissivity	Daily	1000 m
	MCD15A3H	LAI and FPAR	4-Day	500 m
MODIS/Combined	MCD19A2	Aerosol optical depth (AOD)	Daily	1000 m
	MCD12Q1	Land cover	Yearly	500 m
		Air temperature (T_a)		
		Incoming surface radiation		
ERA5	ECMWF	Total columnar water vapor (TCWV)	Daily	27,830 m
		Atmospheric pressure (P)		
		Wind speed at 10 m height (u)		
SRTM		Elevation	Yearly	90 m

2.2.2. Flux Towers

Eddy covariance (EC) flux measurements from the FLUXNET2015 "http://fluxnet.fluxdata.org/data/fluxnet2015-dataset (accessed on 27 January 2022)" dataset and ICOS (Warm Winter 2020 ecosystem eddy covariance flux data in FLUXNET-Archive format—release 2022-1 (Version 1.0), "https://doi.org/10.18160/2G60-ZHAK (accessed on 1 January 2022)" were used to evaluate the model. From those datasets, 11 flux stations covering a wide altitudinal range were selected. The flux tower data were selected based on having required variables, including daily flux components (Rn, LE, H, and G) and precipitation. Daily LE was converted to units of mass flux (mm·day^{-1}) for the ET_d model comparison.

The location of selected flux towers is shown in Figure 1, and additional details about each flux tower are presented in Table 2.

Table 2. Detailed information of selected flux towers. The height of the temperature measurement (z_T). The height of the wind measurement (z_U). The International Geosphere–Biosphere Programme (IGBP) defines landcover type. Savanna (SAV), Woody savanna (WSA), cropland (CRO), evergreen broadleaf forest (EBF), open shrubland (OSH).

Flux ID	Latitude	Longitude	Altitude	z_T	z_U	IGBF	Study Period
ES_Abr	38.70	−6.79	279	2/12	12	SAV	2015–2020
ES_LM1	39.94	−5.78	266	2/15	15	SAV	2014–2020
ES_LM2	39.93	−5.78	270	2/15	15	SAV	2014–2020
ES_Cnd	37.91	−3.23	366	6	9.3	WSA	2014–2020
FR_Aur	43.55	1.11	250	2	2	CRO	2005–2020
FR_Lam	43.50	1.24	181	2	2	CRO	2005–2020
FR_Pue	43.74	3.60	270	10	10	EBF	2000–2014
ES_LgS	37.01	−2.97	2267	1.2	2.8	OSH	2007–2009
ES_Agu	36.94	−2.03	195	3.28	3.28	OSH	2006–2020
ES_LJu	36.93	−2.75	1600	2.5	2.5	OSH	2004–2020
ES_Amo	36.83	−2.25	58	2.9	2.9	OSH	2007–2012

To evaluate the modeled ET_d, flux tower data were screened according to a daily energy closure >0.65 and with no precipitation present. The energy balance closure (EBC) was used to evaluate the reliability of the EC measurements at flux towers [46,49]. The EBC formulation is based on the first law of thermodynamics, representing that the sum of turbulent fluxes (LE, H) is equal to the available energy (Rn, G, and heat storage (S)), as follows:

$$EBC = \frac{\sum(H + LE)}{\sum(R_n - G - S)} \tag{1}$$

Therefore, the ideal EBC is close to 1 and the lack of closure increases uncertainty in ET measurements [50,51].

Numerous studies have shown imbalances in the ratio of turbulent fluxes to available energy in the EC technique [49,52]. The Bowen ratio method [53] and residual method are two standard methods used for enforcing the EBC in the EC observations by attributing available energy to turbulent fluxes. In the current study, a distribution of the residual according to the Bowen ratio method (LE$_{BR}$) was applied as suggested by [53,54]. In addition, LE was recalculated as the residual (LE$_{RES}$) of the surface energy budget used in previous TSEB evaluations [55]; and both closure methods were then used to evaluate ET$_d$.

On clear-sky days, the maximum shortwave radiation peak occurs at local solar noon and reduces to zero at night. Hence, clear-sky observations were identified by calculating the ratio of incoming shortwave radiation to potential incoming shortwave radiation. Days with a ratio exceeding 70% were visually inspected, and those meeting this criterion were selected as clear-sky observations [56].

2.3. Overall Modeling Framework

A modeling framework for estimating ET$_d$ based on the SEN-ET model (detailed description can be found at "https://www.esa-sen4et.org (accessed on 19 March 2023)", calculating the SEB through the TSEB model [28] (see Section 2.4 "*TSEB model overview*"), was refined for Terra/Aqua MODIS data (Figure 2).
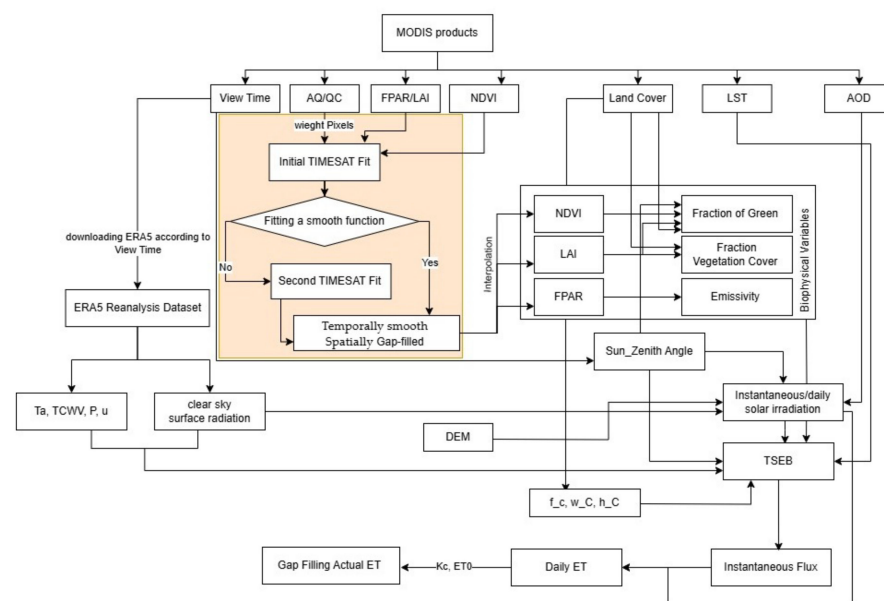

Figure 2. Flowchart of the modeling framework estimating ET$_d$ time series. The orange rectangle denotes the pre-processing of MODIS vegetation indices through TIMESAT.

The SEN-ET model was designed to use Sentinel-2 and Sentinel-3 data as well as ERA5 reanalysis data as TSEB model inputs. To refine this methodology for Terra/Aqua MODIS data, several MODIS products (see Table 1) were used to obtain biophysical variables, vegetation properties, and surface characteristics. TIMESAT 3.3 [53] was employed to temporally smooth and spatially complete the MODIS normalized difference vegetation index (NDVI), leaf area index (LAI), and fraction of photosynthetically active radiation (FPAR). This smoothing process transforms noisy signals (due to clouds and other atmospheric and image acquisition artifacts) into smooth seasonal curves through a weighting mechanism and quality control (QC) layers of MODIS products. A double logistic smoothing method was selected, as it provided a better fit to the data, as suggested by [57].

As in the original SEN-ET model, meteorological data including air temperature, atmospheric vapor pressure, wind speed above the canopy, atmospheric pressure, and

total column water vapor (see Table 1) were downloaded from the ERA5 reanalysis dataset. Meteorological data were interpolated at the satellite overpass through the view time layers of Terra/Aqua LST products.

Land cover data were used to parameterize TSEB surface characteristics (see Table 3). Instantaneous and daily incoming shortwave radiation were estimated using DEM, water vapor, and aerosols from MERRA-2 [58].

Table 3. LUT utilized to run the TSEB model for extracting the structural parameters of vegetation according to land cover type. H_C represents the maximum canopy height considered for this study (m) (see Appendix A); Ω denotes the clustering level of the canopy.

Category	H_C	Ω
Evergreen Needleleaf Forest	20	1
Evergreen Broadleaf Forest	10	1
Deciduous Broadleaf Forest	10	1
Mixed Forests	15	1
Closed Shrublands	1.5	1
Open Shrublands	1.5	0.15
Woody Savannas	8	0.75
Savannas	8	0.25
Grasslands	0.5	1
Permanent Wetlands	10	1
Croplands	1.2	1
Urban and Built-Up Land	20	0
Cropland/Natural Vegetation Mosaic	1.2	0.5
Snow and Ice	0	0
Barren or Sparsely Vegetated Land	0.05	1
Water	0	0

After resampling all input data to a 1 km spatial resolution, the instantaneous ET was estimated using the TSEB model. The instantaneous ET was then upscaled to ET_d. Finally, gap-filling methods were applied to estimate ET_d on clouds or low-quality data based on MODIS QC (2.5 "*Temporal upscaling and gap-filling methods*").

2.4. TSEB Model Overview

To estimate surface energy fluxes, the Two-Source Energy Balance (TSEB) model in its series version, based on the Priestley–Taylor approximation (TSEB-PT) introduced by [28] and further developed by [59,60], was used (see Figure 3). The model considers the surface radiometric temperature (T_{RAD}), either measured from field-based radiometers or from satellite thermal sensors (LST), to be a composite of both soil (T_S) and canopy (T_C) temperatures, weighted by the fraction of vegetation (f_C) observed at a certain radiometer or thermal sensor viewing angle (θ):

$$T_{RAD}(\theta) \approx \left[f_C(\theta) T_C^4 + \left(1 - f_C(\theta)\right) T_S^4 \right]^{0.25} \tag{2}$$

where $f_C(\theta)$ is the fraction of vegetation observed at a zenith angle θ defined by the following:

$$f_c(q) = 1 - exp\left(\frac{-0.5 W LAI}{cos q} \right) \tag{3}$$

where the factor Ω indicates the clustering level of the canopy [27] (see Table 3 for value definition used in this study). T represents temperature (K). The subscripts C and S denote the canopy and soil components, respectively. The surface structural characteristics were parameterized into the Look-Up Table (LUT) presented in Table 3 to accurately model the different fractions of the surface covered by the canopy f_c according to the land cover type.
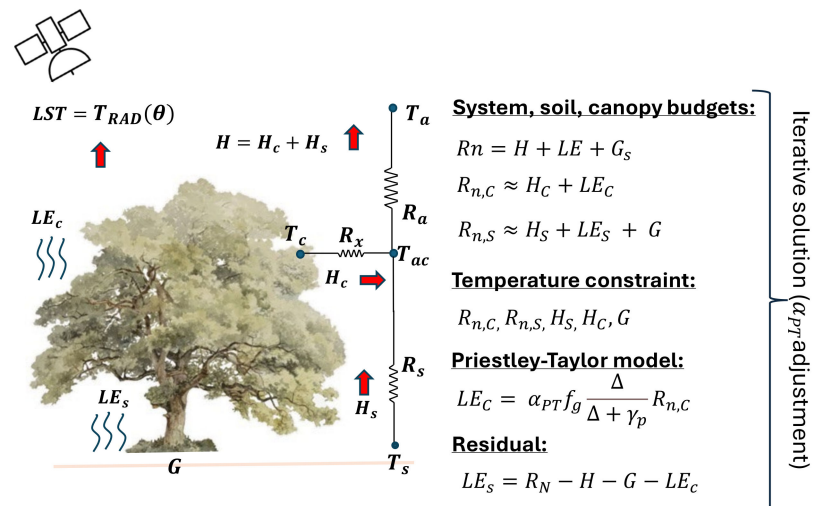
Figure 3. TSEB modelling scheme (adapted from [61]).

The model contributes to partitioning the surface energy fluxes and radiometric land surface temperature (T_{RAD}) between vegetation and soil sources to estimate instantaneous R_n, H, and G. Consequently, instantaneous LE can be calculated as the residual of the SEB (Equations (4)–(6)):

$$LE = R_n - H - G \tag{4}$$

$$R_{n,C} \approx H_C + LE_C \tag{5}$$

$$R_{n,S} \approx H_S + LE_S + G \tag{6}$$

R_n is estimated as the sum of net shortwave and longwave radiation above the canopy. Net shortwave radiation is determined using incoming solar radiation and surface albedo, while net longwave radiation is calculated using air temperature and LST via the Stefan–Boltzman equation based on atmospheric emissivity [62]. Additionally, G is estimated as 35% of the net soil radiation ($R_{n,S}$) [28,63].

H is calculated from the temperature gradients between the aerodynamic temperature (T_A), the temperature of the soil (T_S), and the temperature of the canopy (T_C), respectively (Equations (7) and (8)):

$$H_S = \rho C_P \frac{T_S - T_{AC}}{R_S} \tag{7}$$

$$H_c = \rho C_p \frac{T_C - T_{AC}}{R_X} \tag{8}$$

And the total sensible heat flux is calculated by Equation (9):

$$H_S + H_C = \rho C_P \frac{T_{AC} - T_A}{R_A} \tag{9}$$

where ρ is the air density (kg m^{-3}), C_P is the specific heat of air (assumed constant at 1013 J kg^{-1} K^{-1}), T_S and T_C are soil and canopy radiometric temperature (K), respectively. T_A is the air temperature in the surface layer measured at some height above the canopy (K), T_{AC} is the temperature in the canopy air space (K), R_S is the resistance to heat flow in the boundary layer immediately above the soil surface (s m^{-1}), R_X is the total boundary layer resistance of the complete canopy leaves (s m^{-1}), and R_A is the aerodynamic resistance (s m^{-1}). Further information on the resistance formulation is given in Appendix A.

The canopy latent heat (LE_C) is estimated following the Priestley–Taylor formula [33,64], initially assuming a potential rate for LE_C, and soil latent heat (LE_S) is solved as a residual as follows:

$$LE_C = \alpha_{PT} f_g \frac{\Delta}{\Delta + \gamma_p} R_{n,C} \tag{10}$$

$$LE_s = R_N - H - G - LE_c \tag{11}$$

where α_{PT} is the Priestley–Taylor coefficient, initially set to 1.26 [64,65], f_g is the fraction of LAI that is green or actively transpiring, Δ is the slope of the saturation vapor pressure versus air temperature curve, and γ_p is the psychometric constant (≈ 66 Pa K^{-1}).

The green vegetation fraction (f_g) is calculated according to [66] using LAI and FPAR biophysical variables:

$$f_g = \frac{fAPAR}{fIPAR} \tag{12}$$

where the fraction of intercepted photosynthetically active radiation ($fIPAR$) is estimated depending on the Sun zenith angle (SZA):

$$fIPAR = 1 - exp\left(\frac{-0.5\,LAI}{\cos(SZA)}\right) \tag{13}$$

Under stress conditions, LE_C is iteratively recalculated to reduce the α_{PT} value [28,29]. To estimate the LE flux from the canopy component, the TSEB internally changes its initial α_{PT} values of 1.26 to allow an acceptable partitioning between LE_C and LE_S under stressed vegetation conditions. The initial value of α_{PTC} is down-adjusted when the TSEB results in negative values for LE_S, given that condensation on the soil is unlikely to occur during the day [28]. This condition typically occurs if the potential transpiration flux is too high to be consistent with the observed surface temperature. The canopy temperature estimation is too low, resulting in a high soil temperature derived from Equation (1). This leads to high soil sensible heat (Equation (5)) exceeding the available energy at the soil surface; hence, $LE_S < 0$ result from Equation (13). When this non-physical condition is encountered midday, it is assumed that the canopy is stressed and α_{PT} is iteratively reduced until the LE_S values are higher than 0. This iterative scheme works well in ecosystems where canopy values of α_{PTC} are relatively conservative under unstressed conditions [66,67], while for stressed canopies where the soil surface is usually dry, a LE_S value close to zero is a reasonable assumption [40,68].

2.5. Temporal Upscaling and Gap-Filling Methods

The instantaneous ET was upscaled by means of the ratio between instantaneous LE_i estimated by the model and the ratio between instantaneous (SI_i) and daily (SI_d) solar irradiance:

$$ET_d = SI_d \frac{LE_i}{SI_i} \tag{14}$$

ET_d is converted to units of mass flux (mm·day^{-1}) through Equation (15):

$$ET_d = \frac{LE_i}{P_w \lambda} 10^3\,86,400 \tag{15}$$

where P_w (kg.m^{-3}) is the density of air-free water at a pressure of 101.325 kPa, λ (J.kg^{-1}) is the latent heat of vaporization, λE is in W·m^{-2}, and the conversion factors 10^3, 86,400 are in mm·m^{-1} and s·h^{-1}, respectively.

The gap in the ET_d time series due to cloud presence or low-quality satellite observations according to MODIS QC flags was filled using the ratio of actual ET and potential ET (ET_a/ET_0) at the objective date (i.e., the date of the pixel that needs to be gap-filled) and closest valid actual ET output within 10 days of the objective date [69].

2.6. Model Evaluation

The modeled ET_d estimated through the modeling framework adapted for MODIS data was evaluated against data collected from 11 flux towers. Certain dates were omitted from the analysis due to the following reasons: (a) absence of MODIS LST data over the towers because of cloud cover or sensor malfunctions; (b) presence of rainfall; (c) gaps in the flux tower dataset; and (d) instances where energy closure fell below 0.65.

The TSEB model performance was evaluated by the following metrics: Pearson correlation coefficient (r, Equation (16)), the root mean square error (RMSE, Equation (17)), and the mean bias error (MBE, Equation (18)).

$$r = \frac{\sum_{i=1}^{n} \left(E_i - \overline{E}\right)\left(O_i - \overline{O}\right)}{\left[\sum_{l=1}^{N}\left(O_i - \overline{O}\right)^2\right]^{0.5}\left[\sum_{l=1}^{N}\left(E_i - \overline{E}\right)^2\right]^{0.5}} \tag{16}$$

$$RMSE = \sqrt{\frac{\sum_{i=1}^{n}(E_i - O_i)^2}{n}} \tag{17}$$

$$BIAS = \frac{\sum_{i=1}^{n}(E_i - O_i)}{n} \tag{18}$$

where n is the number of observations, O_i is the observed value (in situ measurements acquired by the flux stations), E_i is the estimated value with the model, $\overline{O}$ is the average of measured values, and $\overline{E}$ is the average of estimated values.

2.7. LST Evaluation

The LST is a critical variable for estimating ET using the thermal-based TSEB model [7, 24]. Thus, to evaluate its impact on the TSEB model, the accuracy of LST products was evaluated by comparing the LST derived from MODIS with those calculated using half-hourly longwave incoming and outgoing radiance measured from the net radiometer sensor at each flux tower at the times of the Terra and Aqua satellite overpasses, approximately 11:00 a.m. and 1:00 p.m. local solar time, respectively. The LST at the flux tower sites was calculated using Equation (19):

$$LST_p = \left(\frac{L_{up} - (1 - \varepsilon)\, L_{down}}{\varepsilon\sigma}\right)^{1/4} \tag{19}$$

where L_{up} and L_{down} are the longwave outgoing and incoming radiance, respectively. σ is the Stefan–Boltzmann's constant (5.67×10^{-8} W·m^{-2}·K^{-4}) and p the subscript refers to the pyrgeometer. ε is the broadband emissivity that was estimated using spectral emissivity LST in bands 31 and 32 from the LST and emissivity MODIS product (MOD11A1), according to [70] following:

$$\varepsilon = 0.4857\varepsilon_{31} + 0.5414\varepsilon_{32} \tag{20}$$

3. Results

3.1. Flux Tower EBC Screening Results

Flux tower EBC and R^2 values were lower when considering the entire dataset, with the EBC ranging from 0.68 to 1 and R^2 from 0.41 to 0.95 (top left box in each panel of Figure 4). Additionally, at all sites, the EC method tended to underestimate the energy flux components (H+LE), with the largest underestimation—up to 0.43—occurring at ES_LgS (IGBP OSH). However, after screening data were used to impose an EBC > 0.65 and with no precipitation present, the mean EBC and R^2 values improved significantly to 0.99 and 0.94, respectively. This indicated that the screened EC flux tower data were robust for evaluating the proposed modeling framework. After screening the dataset, a total number of 19265 EC observations for the whole flux tower dataset were available for model evaluation.

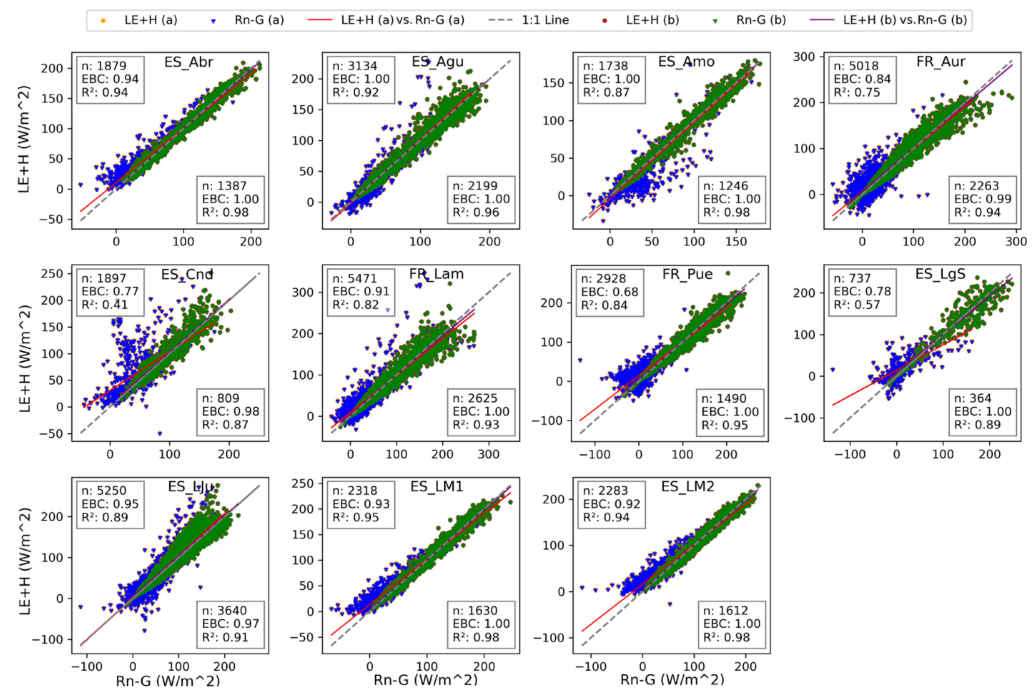This EC dataset was then split into clear-sky and all-sky observations for Terra and Aqua (Tables 4–6).

Figure 4. Scatterplots of the EBC calculated using the EC with the statistical metrics for the entire study period (**top left**) and the days compared with the mode (**bottom right**) at each flux tower.

Table 4. Statistical metrics between the ET_d estimated under clear-sky observations with Terra and Aqua (in italic) datasets were compared against unclosed ET, ET_{BR}, and ET_{RES} calculated using the EC method at flux towers (metrics include MBE and mean RMSE, both measured in mm·day^{-1}). * means that the Pearson correlation was not statistically significant with an $\alpha = 0.05$.

Flux ID	n	Model LE vs. Unclosed LE			Model LE vs. LE$_{BR}$			Model vs. LE$_{RES}$		
Terra | Aqua		MBE	RMSE	r	MBE	RMSE	r	MBE	RMSE	r
ES_Abr	552 | 544	−0.91 | 0.60	1.23 | 0.97	0.65 | 0.72	−0.89 | 0.53	1.22 | 0.93	0.65 | 0.72	−0.84 | 0.58	1.17 | 0.96	0.66 | 0.72
ES_LM1	770 | 766	0.41 | 0.41	0.99 | 1.01	0.74 | 0.72	0.35 | 0.35	1.00 | 1.02	0.73 | 0.71	0.30 | 0.30	0.98 | 0.99	0.73 | 0.71
ES_LM2	759 | 755	0.40 | 0.56	0.91 | 0.84	0.77 | 0.80	0.35 | 0.48	0.90 | 0.84	0.77 | 0.80	0.31 | 0.36	0.88 | 0.82	0.77 | 0.76
ES_Cnd	307 | 299	0.91 | 0.71	1.40 | 0.94	0.66 | 0.68	0.79 | 0.58	1.21 | 0.86	0.64 | 0.67	0.61 | 0.39	1.03 | 0.81	0.60 | 0.62
FR_Aur	668 | 674	1.27 | 1.17	1.88 | 1.78	0.57 | 0.60	1.14 | 1.05	1.85 | 1.75	0.56 | 0.58	1.07 | 0.98	1.78 | 1.68	0.58 | 0.60
FR_Lam	465 | 461	1.07 | 0.78	1.88 | 1.71	0.52 | 0.53	0.95 | 0.65	1.85 | 1.69	0.52 | 0.53	0.88 | 0.57	1.80 | 1.66	0.53 | 0.53
FR_Pue	534 | 529	1.44 | 0.56	1.92 | 1.58	0.53 | 0.42	1.39 | 0.51	1.89 | 1.56	0.53 | 0.43	1.31 | 0.43	1.82 | 1.50	0.55 | 0.45
ES_LgS	236 | 218	1.67 | 1.77	1.91 | 1.95	0.66 | 0.66	1.59 | 1.69	1.84 | 1.88	0.64 | 0.65	1.45 | 1.56	1.76 | 1.80	0.60 | 0.61
ES_Agu	186 | 178	1.82 | 1.54	1.93 | 1.70	0.08 * | 0.11 *	1.79 | 1.52	1.91 | 1.66	0.07 * | 0.11 *	1.65 | 1.37	1.80 | 1.54	0.03 * | 0.14 *
ES_LJu	760 | 753	0.77 | 0.42	1.25 | 1.09	0.47 | 0.40	0.71 | 0.36	1.22 | 1.08	0.47 | 0.40	0.52 | 0.17	1.30 | 1.07	0.48 | 0.39
ES_Amo	467 | 453	1.03 | 0.67	1.37 | 1.09	0.33 | 0.42	1.01 | 0.66	1.36 | 1.08	0.32 | 0.41	0.94 | 0.59	1.32 | 1.07	0.27 | 0.34
Total/Average	5704 | 5630	0.90 | 0.83	1.51 | 1.33	0.61 | 0.55	0.83 | 0.76	1.48 | 1.30	0.54 | 0.55	0.74 | 0.66	1.42 | 1.26	0.53 | 0.53

Table 5. Statistical metrics between the ET_d estimated using the TSEB model for all-sky observations and gap-filled data (in italic) with Terra dataset were compared against unclosed ET, ET_{BR}, and ET_{RES} calculated using the EC method at flux towers (metrics include MBE and mean RMSE, both measured in mm·day^{-1}. All Pearson correlations were statistically significant with an $\alpha = 0.05$.

Flux ID	n	Model LE vs. Unclosed LE			Model LE vs. LE$_{BR}$			Model vs. LE$_{RES}$		
Terra		MBE	RMSE	r	MBE	RMSE	r	MBE	RMSE	r
ES_Abr	1030 | *1387*	1.02 | *1.02*	1.31 | *1.27*	0.63 | *0.69*	1.00 | *0.74*	1.3 | *1.09*	0.63 | *0.69*	0.95 | *0.69*	1.25 | *1.01*	0.64 | *0.69*
ES_LM1	1249 | *1630*	0.56 | *0.56*	1.06 | *1.05*	0.71 | *0.74*	0.51 | *0.52*	1.05 | *1.04*	0.72 | *0.73*	0.46 | *0.47*	1.02 | *0.98*	0.71 | *0.73*
ES_LM2	1237 | *1612*	0.58 | *0.52*	1.02 | *0.93*	0.72 | *0.75*	0.54 | *0.56*	1.01 | *0.98*	0.72 | *0.75*	0.49 | *0.51*	0.98 | *0.91*	0.72 | *0.75*
ES_Cnd	695 | *809*	1.04 | *0.40*	1.31 | *0.88*	0.57 | *0.67*	1.71 | *0.78*	1.25 | *1.33*	0.56 | *0.58*	1.83 | *0.66*	1.18 | *1.15*	0.55 | *0.59*
FR_Aur	1280 | *2263*	1.40 | *1.39*	1.91 | *1.84*	0.61 | *0.62*	1.29 | *1.37*	1.87 | *1.97*	0.6 | *0.61*	1.22 | *1.31*	1.79 | *1.87*	0.62 | *0.62*
FR_Lam	1470 | *2625*	1.04 | *0.91*	1.77 | *1.60*	0.62 | *0.63*	0.94 | *0.94*	1.73 | *1.57*	0.62 | *0.63*	0.88 | *0.94*	1.69 | *1.60*	0.63 | *0.64*
FR_Pue	1066 | *1490*	1.67 | *3.67*	2.14 | *4.22*	0.53 | *0.48*	1.61 | *3.69*	2.1 | *4.24*	0.53 | *0.47*	1.54 | *3.72*	2.03 | *4.26*	0.55 | *0.46*
ES_LgS	282 | *364*	1.83 | *1.97*	2.08 | *2.16*	0.59 | *0.62*	1.75 | *1.98*	2.02 | *2.19*	0.6 | *0.60*	1.62 | *2.06*	1.94 | *2.35*	0.55 | *0.56*
ES_Agu	1636 | *2199*	1.88 | *1.55*	2.06 | *1.73*	0.07 | *0.13*	1.86 | *1.56*	2.04 | *1.73*	0.06 | *0.12*	1.75 | *1.54*	1.94 | *1.74*	0.12 | *0.18*
ES_LJu	2814 | *3640*	1.07 | *0.83*	1.47 | *1.30*	0.41 | *0.42*	1.01 | *1.07*	1.42 | *2.12*	0.41 | *0.42*	0.80 | *0.88*	1.3 | *1.82*	0.41 | *0.41*
ES_Amo	1002 | *1246*	1.42 | *1.07*	1.74 | *1.41*	0.14 | *0.16*	1.41 | *1.37*	1.74 | *2.83*	0.12 | *0.15*	1.34 | *1.31*	1.69 | *2.69*	0.10 | *0.12*
Total/Average	13,761 | *19,265*	1.22 | *1.26*	1.62 | *1.67*	0.51 | *0.54*	1.24 | *1.32*	1.59 | *1.92*	0.51 | *0.52*	1.17 | *1.28*	1.53 | *1.85*	0.51 | *0.52*
Average all-sky observations and gap-filled data		1.24	1.64	0.52	1.28	1.75	0.51	1.22	1.69	0.51

Table 6. Statistical metrics between the daily ET estimated using the TSEB model for all-sky observations and gap-filled data (in italic) with Aqua dataset were compared against unclosed ET, ET_{BR}, and ET_{RES} calculated using the EC method at flux towers (metrics include MBE and mean RMSE, both measured in mm·day^{-1}). All Pearson correlations were statistically significant with an $\alpha = 0.05$.

Flux ID	n	Model LE vs. Unclosed LE			Model LE vs. LE$_{BR}$			Model vs. LE$_{RES}$		
Aqua		MBE	RMSE	r	MBE	RMSE	r	MBE	RMSE	r
ES_Abr	992 | *1387*	0.77 | *0.76*	1.10 | *1.06*	0.66 | *0.67*	0.7 | *0.99*	1.04 | *1.58*	0.67 | *0.67*	0.75 | *0.94*	1.09 | *1.47*	0.66 | *0.68*
ES_LM1	1238 | *1630*	0.57 | *0.58*	1.09 | *1.03*	0.68 | *0.71*	0.52 | *0.50*	1.08 | *1.09*	0.67 | *0.70*	0.47 | *0.45*	1.05 | *1.02*	0.67 | *0.71*
ES_LM2	1225 | *1612*	0.52 | *0.60*	0.96 | *1.01*	0.74 | *0.77*	0.48 | *0.47*	0.95 | *0.83*	0.74 | *0.77*	0.43 | *0.43*	0.92 | *0.78*	0.74 | *0.77*
ES_Cnd	684 | *809*	0.85 | *0.59*	1.12 | *0.98*	0.56 | *0.62*	0.76 | *0.57*	1.07 | *1.00*	0.55 | *0.55*	0.63 | *0.45*	1.01 | *0.88*	0.53 | *0.57*
FR_Aur	1304 | *2263*	1.34 | *1.47*	1.85 | *1.92*	0.61 | *0.62*	1.23 | *1.28*	1.81 | *1.89*	0.6 | *0.61*	1.16 | *1.22*	1.74 | *1.81*	0.62 | *0.63*
FR_Lam	1449 | *2625*	0.82 | *1.15*	1.64 | *1.77*	0.62 | *0.63*	0.72 | *1.18*	1.62 | *1.74*	0.62 | *0.63*	0.66 | *0.18*	1.58 | *1.77*	0.63 | *0.64*
FR_Pue	1017 | *1490*	0.94 | *3.45*	1.77 | *4.01*	0.44 | *0.47*	0.89 | *3.47*	1.75 | *4.02*	0.44 | *0.46*	0.82 | *3.50*	1.69 | *4.05*	0.45 | *0.49*
ES_LgS	242 | *364*	1.89 | *1.87*	2.08 | *2.11*	0.61 | *0.62*	1.81 | *1.88*	2.02 | *2.13*	0.6 | *0.59*	1.68 | *1.96*	1.94 | *2.29*	0.56 | *0.54*
ES_Agu	1552 | *2199*	1.63 | *1.80*	1.82 | *1.97*	0.05 | *0.13*	1.62 | *1.80*	1.81 | *1.97*	0.05 | *0.12*	1.50 | *1.79*	1.71 | *1.97*	0.09 | *0.15*
ES_LJu	2662 | *3640*	0.75 | *1.12*	1.27 | *1.49*	0.33 | *0.36*	0.69 | *0.78*	1.24 | *1.61*	0.34 | *0.36*	0.48 | *0.59*	1.19 | *1.47*	0.36 | *0.33*
ES_Amo	964 | *1246*	1.09 | *1.39*	1.46 | *1.69*	0.23 | *0.27*	1.08 | *1.05*	1.48 | *1.95*	0.1 | *0.26*	1.02 | *0.99*	1.45 | *1.86*	0.06 | *0.23*
Total/Average	13,329 | *19,265*	1.01 | *1.34*	1.47 | *1.73*	0.50 | *0.53*	0.95 | *1.27*	1.44 | *1.80*	0.49 | *0.52*	0.87 | *1.36*	1.40 | *1.76*	0.49 | *0.52*
Average all-sky observations and gap-filled data		1.17	1.60	0.51	1.11	1.62	0.50	1.11	1.58	0.5

3.2. Evaluation of Modeled ET_d Under Clear-Sky Observations

The total number of clear-sky observations (with available LST) were 5704 and 5630 for Terra and Aqua, respectively (Table 4). The model evaluation with both closed and unclosed datasets showed better performance in comparison with all-sky observations and gap-filled data (see Tables 5 and 6). The modeled ET_d showed the lowest errors with ET_{RES}, achieving an MBE of 0.74 mm·day^{-1} and 0.66 mm·day^{-1} for Terra and Aqua, respectively, and with an average RMSE of 1.42 mm·day^{-1} and 1.26 mm·day^{-1}, for Terra and Aqua, respectively.

It is important to remark that around 30% of the EC dataset is under clear-sky observations. Thus, this limitation was addressed by applying the gap-filling method with solar radiation modelling under all-sky observations, including both clear-sky and cloudy observations.

3.3. Evaluation of Modeled ET_d with All-Sky Observations and Gap-Filled Data

The results demonstrated an agreement between the modeled ET_d and measured ET_d (Figure 5 and in detail in Tables 5 and 6). The model effectively captured both the spatial and temporal variations in ET_d across various IGBP classifications. However, it is notable that the model, using both Terra and Aqua datasets, tended to overestimate ET_d.

This finding is consistent with previous studies, which have reported that TSEB models may overestimate ET, likely due to inaccurate assumptions about the fraction of green vegetation [6,71,72].
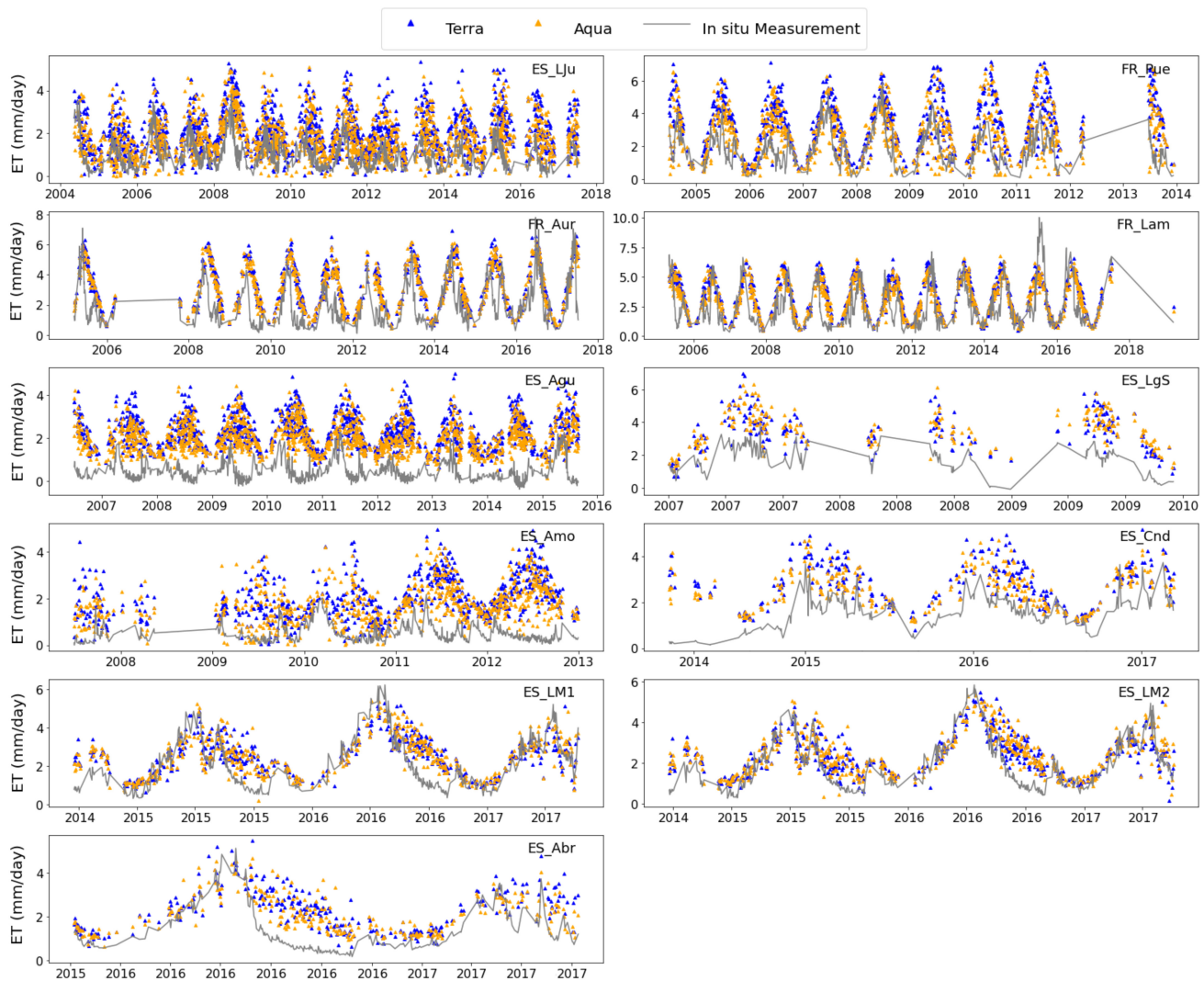

Figure 5. Temporal variations in the modeled ET_d estimated using Terra and Aqua datasets compared to in situ-measured ET at flux towers.

Regarding all-sky observations, the statistical metrics for Terra and Aqua datasets indicated differences between the modeled ET_d and the daily unclosed ET, ET_{BR}, and ET_{RES} (Tables 5 and 6). The modeled ET_d showed the lowest errors with ET_{RES}, with MBE values of 1.17 mm·day^{-1} for Terra and 0.87 mm·day^{-1} for Aqua, and corresponding average RMSE values of 1.53 mm·day^{-1} and 1.40 mm·day^{-1}, respectively. Additionally, the modeled ET_d demonstrated better alignment with ET_{BR} compared to unclosed ET, with MBE and mean RMSE values of 1.24 mm·day^{-1} and 1.59 mm·day^{-1} for Terra, and 0.95 mm·day^{-1} and 1.44 mm·day^{-1} for Aqua. These findings align with existing studies [7]. Notably, the Aqua dataset, with its lower MBE and mean RMSE, demonstrated better performance compared to Terra, primarily due to differences in satellite overpass times. The mean Aqua overpass time is around 13:00 solar local time, when plants are under more water stress, likely contributing to the better performance of the model with the Aqua dataset. The highest correlation between the modeled ET and both closed and unclosed ET was observed at the ES_LM2 site in both datasets. Conversely, the lowest correlation was observed at the ES_Agu and ES_Amo sites. After applying the gap-filling method,

the total number of days compared with flux measurements increased significantly, from 13,761 to 19,265 for Terra and 13,329 to 19,265 for Aqua (Tables 5 and 6). This increase was particularly pronounced at the FR_Lam and FR_Aur sites, where the day numbers grew by approximately 1000 in each dataset. These sites are in the northeastern part of the study area, where cloudy conditions are frequent.

Additionally, the statistical metrics for both Terra and Aqua datasets showed slight changes between the gap-filled modeled ET_d compared to all-sky observations results (Tables 5 and 6). The largest discrepancies between the gap-filled modeled ET_d and in situ ET_d measurements were observed at the FR_Pue site, while the smallest differences occurred at the ES_LM1, ES_LM2, ES_Abr, and ES_Cnd sites in both datasets.

In contrast, the statistical metrics gained from comparing the gap-filled modeled ET_d with the EC flux tower measurements (including unclosed ET, ET_{BR}, and ET_{RES}) showed the lowest errors with unclosed ET. For Terra, the MBE and mean RMSE were 1.26 mm·day^{-1}, 1.67 mm·day^{-1}, and 0.54, respectively, while the corresponding values for Aqua were approximately 1.34 mm·day^{-1} and 1.73 mm·day^{-1}. Notably, the gap-filled modeled ET performed better in the Terra dataset.

Compared to Table 4, the number of clear-sky observations at ES_Agu and ES_LJu sites are significantly lower than that of all-sky observations, accompanied by lower MBE and average RMSE values. This finding indicated that cloudy conditions negatively impact the model's performance at these two sites. In contrast, the results at the FR_Aur site showed no notable changes, likely due to the influence of surface heterogeneity in the model's performance.

Figures 6 and 7 demonstrate that the modeled ET exhibited the strongest correlation with in situ measurements at SAV and CRO sites in both datasets. These simpler land cover types, with less complex vegetation structures and energy balances, appear to align well with the model. In contrast, the modeled ET showed a lower correlation at OSH sites. These sites are characterized by more complex land cover dynamics.

The statistical metrics gained from clear-sky observations showed a lower RMSE and higher agreement compared to all-sky observations and gap-filled data, which reflect that cloudy conditions affect the model's performance significantly.
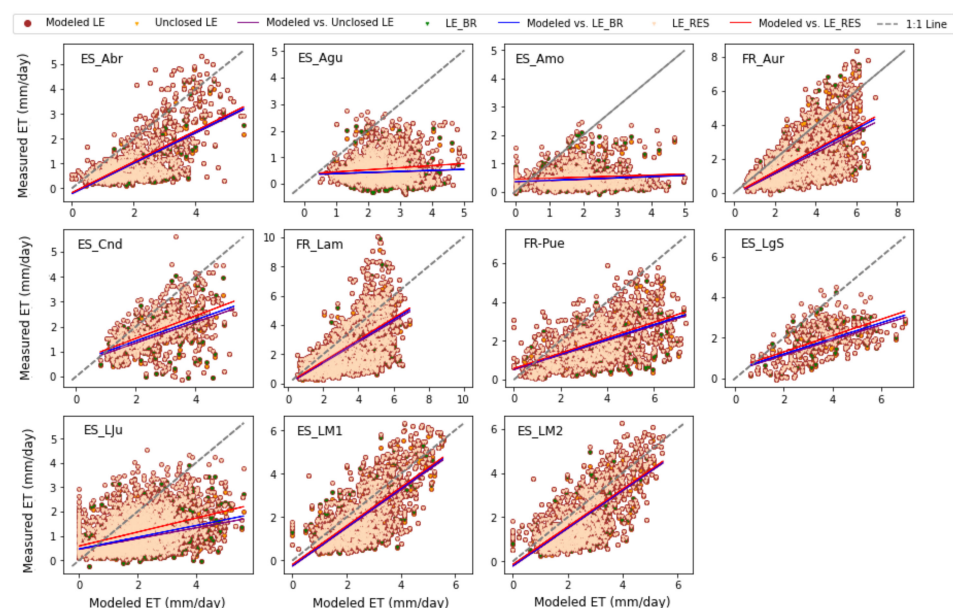

Figure 6. Scatterplots of the modeled ET_d estimated using Terra against unclosed and closed ET (ET_{BR} and ET_{RES}).
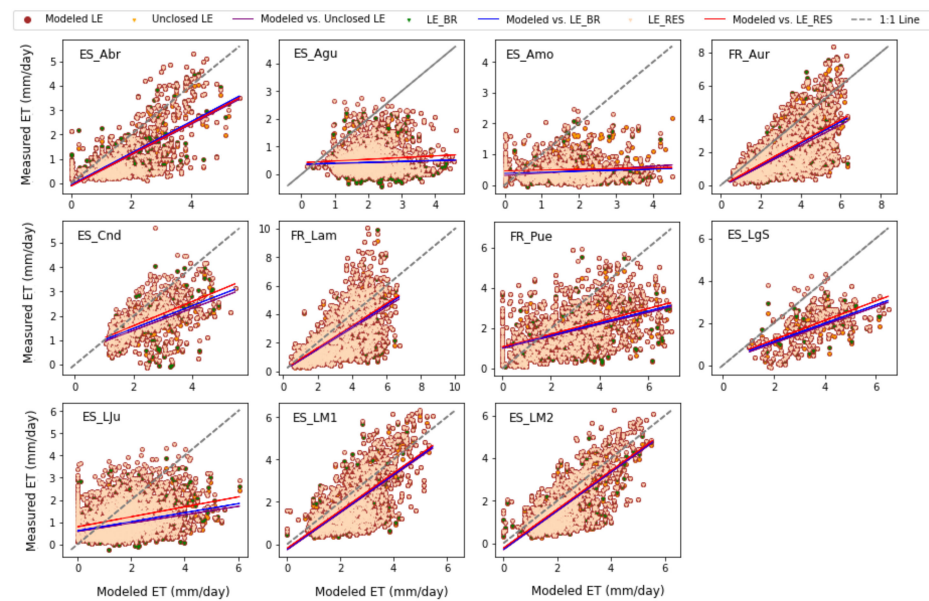
Figure 7. Scatterplots of the modeled ET_d estimated using Aqua against unclosed and closed ET (ET_{BR} and ET_{RES}).

The overall mean results including clear-sky and all-sky observations as well as gap-filled data with Aqua showed the lowest errors with ET_{RES}, by an MBE of 0.96 mm.day^{-1} and an average RMSE of 1.47 mm.day^{-1}, while the equivalent figures for Terra were about 1.06 mm.day^{-1} and 1.60 mm.day^{-1} (Table 7).

Table 7. Overall statistical metrics between the daily ET estimated under clear-sky and all-sky observations as well as gap-filled data with Terra and Aqua (in italic) datasets were compared against unclosed ET, ET_{BR}, and ET_{RES} calculated using the EC method at flux towers (metrics include MBE and mean RMSE, both measured in mm·day^{-1}). All Pearson correlations were statistically significant with an α = 0.05.

Model LE vs. Unclosed LE	Terra/Aqua	MBE	RMSE	r
clear-sky	5704 | *5630*	0.90 | *0.83*	1.51 | *1.33*	0.61 | *0.55*
all-sky	13,761 | *13,329*	1.22 | *1.01*	1.62 | *1.47*	0.51 | *0.50*
gap-filled	19,265 | *19,265*	1.26 | *1.34*	1.67 | *1.73*	0.54 | *0.53*
average		1.13 | *1.06*	1.60 | *1.51*	0.53 | *0.53*
Model LE vs. LEBR	Terra/Aqua	MBE	RMSE	r
clear-sky	5704 | *5630*	0.83 | *0.76*	1.48 | *1.30*	0.54 | *0.55*
all-sky	13,761 | *13,329*	1.24 | *0.95*	1.59 | *1.44*	0.51 | *0.49*
gap-filled	19,265 | *19,265*	1.32 | *1.27*	1.92 | *1.80*	0.52 | *0.52*
average		1.13 | *0.99*	1.66 | *1.51*	0.52 | *0.52*
Model vs. LERES	Terra/Aqua	MBE	RMSE	r
clear-sky	5704 | *5630*	0.74 | *0.66*	1.42 | *1.26*	0.53 | *0.53*
all-sky	13,761 | *13,329*	1.17 | *0.87*	1.53 | *1.40*	0.51 | *0.49*
gap-filled	19,265 | *19,265*	1.28 | *1.36*	1.85 | *1.76*	0.52 | *0.52*
average		1.06 | *0.96*	1.60 | *1.47*	0.52 | *0.51*

3.4. LST Validation

As shown in Figures 8 and 9, the Aqua LST showed better agreement compared with the flux tower LST, with an MBE and mean RMSE of −0.99 K and 2.94 K, respectively, while

for Terra, these values were about −2.60 K and 3.08 K, respectively. Moreover, the highest RMSE was observed at the FR_Lam sites (4.08 K), with an IGBF of CRO in both datasets.
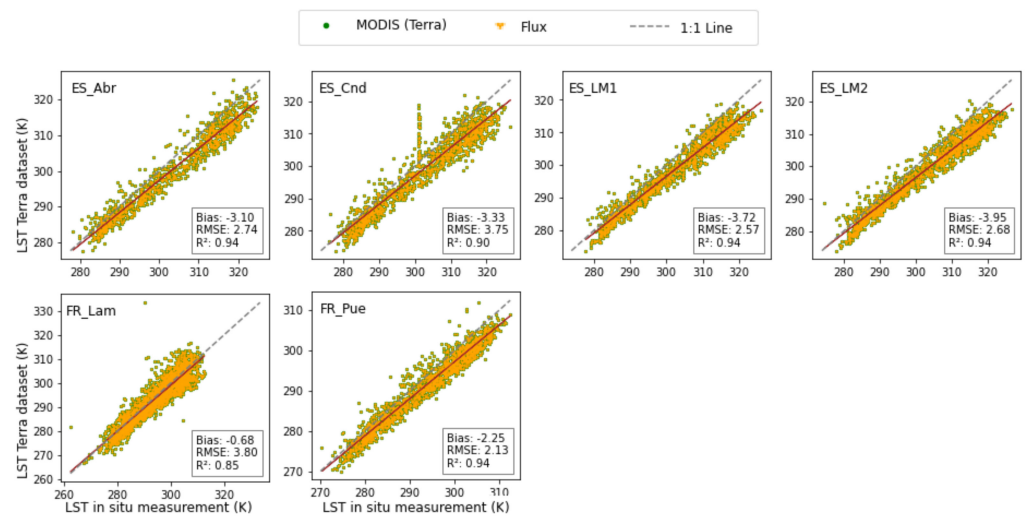

Figure 8. Scatterplots of the LST obtained from MODSI Terra dataset and the LST calculated using half-hourly flux tower data at satellite overpass time.
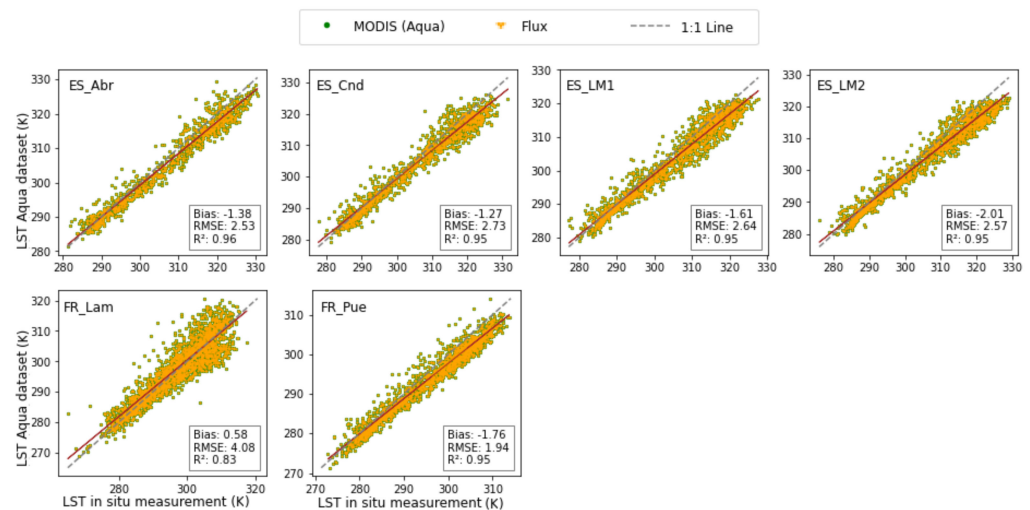

Figure 9. Scatterplots of the LST obtained from MODSI Aqua dataset and the LST calculated using half-hourly flux tower data at satellite overpass time.

3.5. Monthly Variability in Estimated ET from 2000 to 2022 in the Study Area

There are significant variations in the mean monthly ET between the sites due to differences in land cover and climate types (Figures 10 and 11). The highest ET values were observed from May to July in the Terra dataset and from April to July in the Aqua dataset. Furthermore, May and December showed the highest and lowest levels of variability in monthly estimated ET, respectively. The mean monthly ET exhibited the least variability at the ES_Amo site in both Terra and Aqua datasets. Additionally, the most variability in mean monthly ET was observed at the FR_Lam and FR_Aur sites over the time series.
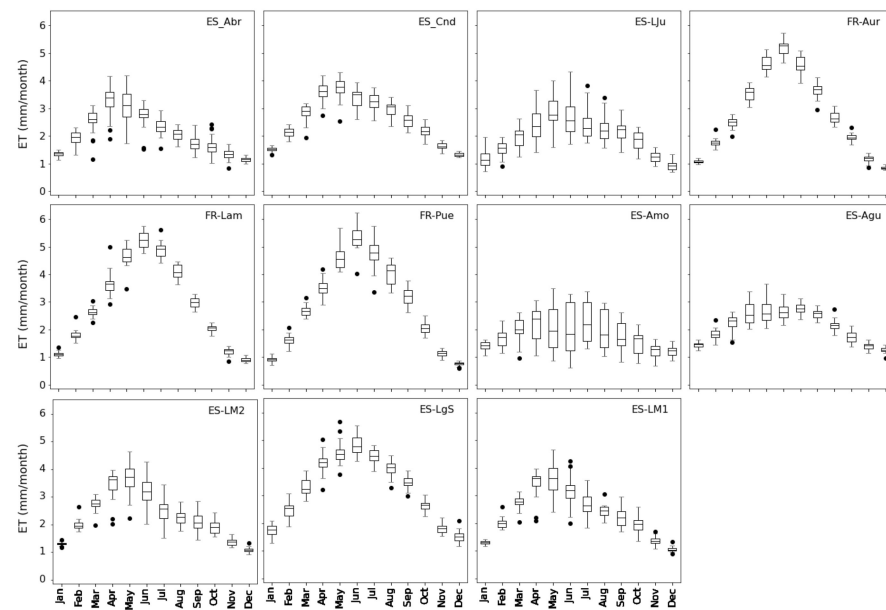
Figure 10. Mean monthly variability in estimated ET using Terra dataset.
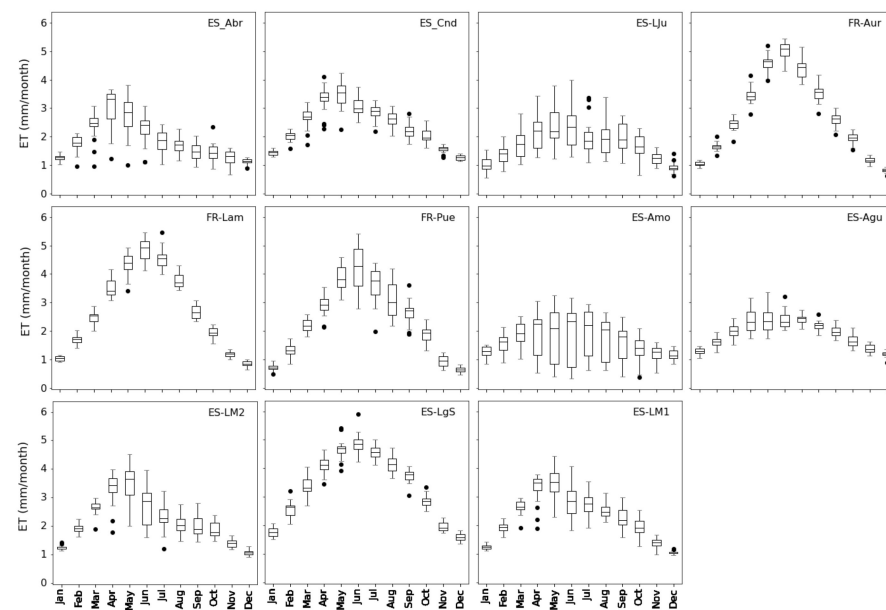
Figure 11. Mean monthly variability in estimated ET using Aqua dataset.

3.6. Seasonal Variability in Estimated ET from 2000 to 2022 in the Study Area

Figures 12 and 13 reveal that seasonal ET shows more variation during the growing seasons (spring and summer) across all sites in both datasets. Additionally, the lowest ET value during the growing seasons was observed at the ES_Amo site, while the highest values were recorded at the ES_LgS and ES_Lam sites.
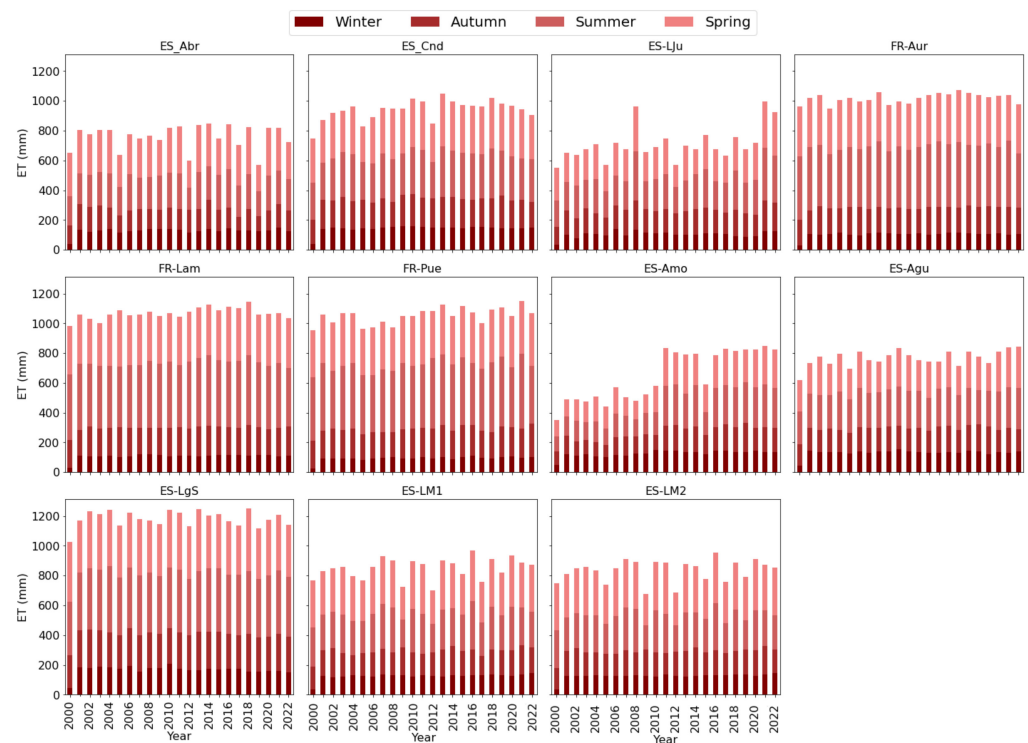
Figure 12. Seasonal variation in estimated ET from 2000 to 2022 in the study area using Terra dataset.
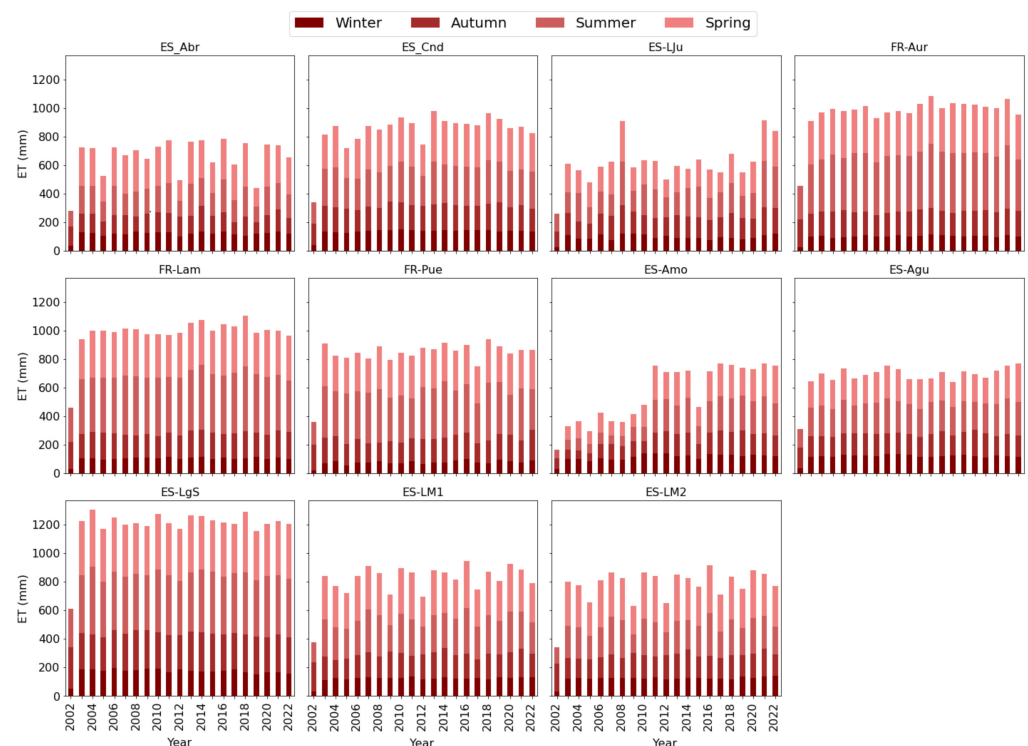
Figure 13. Seasonal variation in estimated ET from 2002 to 2022 in the study area using Aqua dataset.

3.7. Annual Cumulative of Estimated ET from 2000 to 2022 in the Study Area

The highest and lowest mean annual cumulative ET were observed at the CRO and SAV sites, respectively (Figure 14). At the CRO site, the mean ET values were around 1045 mm· year^{-1} and 999 mm·year^{-1} for Terra and Aqua datasets, respectively. Conversely, at the SAV sites, the mean ET was 818 mm/year in the Terra dataset and 767 mm·year^{-1}

in the Aqua dataset. The cumulative ET values exhibited the greatest variability at the OSH sites, ranging from 665 to 1189 mm·year^{-1} for Terra and from 582 to 1221 mm·year^{-1} for Aqua. The mean annual cumulative value of the estimated ET in the WSA site was estimated to be approximately 945 mm·year^{-1} and 868 mm·year^{-1} for Terra and Aqua datasets, respectively, which were higher than the corresponding values at the SAV sites.

Figure 14. Temporal variation in annual cumulative of estimated *ET* from 2000 to 2022 in the study area using Aqua (**left**) and Terra (**right**) dataset.

3.8. Spatiotemporal Variability in Estimated ET from 2000 to 2022 in the Study Area

Figures 15 and 16 highlight significant inter-annual variability in ET from 2000 to 2022, reflecting the complex dynamics of water exchange across the study area. Notably, in 2005, 2009, 2012, and 2022, there were pronounced changes in ET, corresponding to years marked by severe heatwaves and droughts [48]. These fluctuations in ET can largely be attributed to plant water stress, driven by water scarcity, a critical factor in the hydrological cycle.
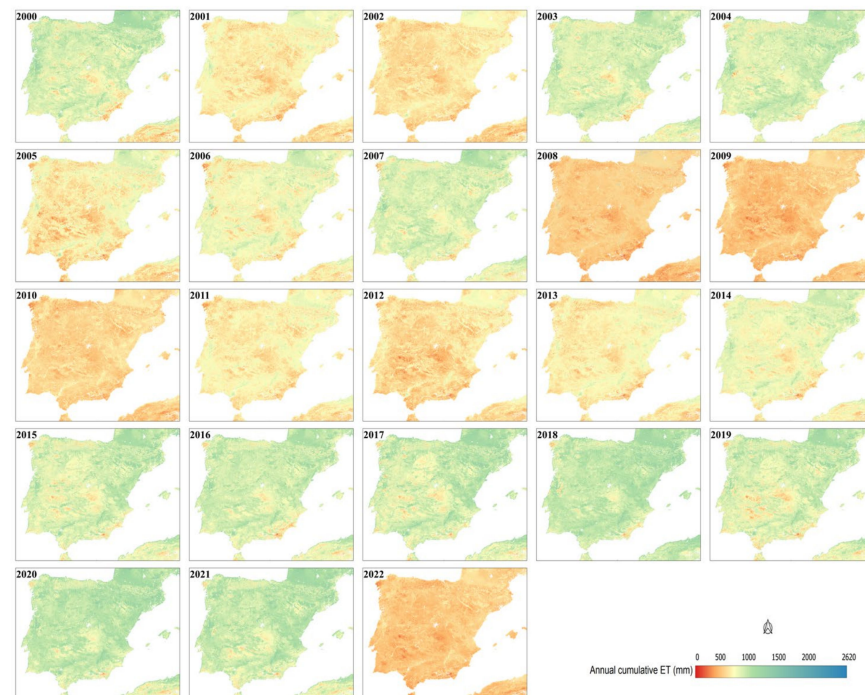
Figure 15. Spatiotemporal variability in annual cumulative of estimated ET from 2000 to 2022 in the study area using Terra dataset.
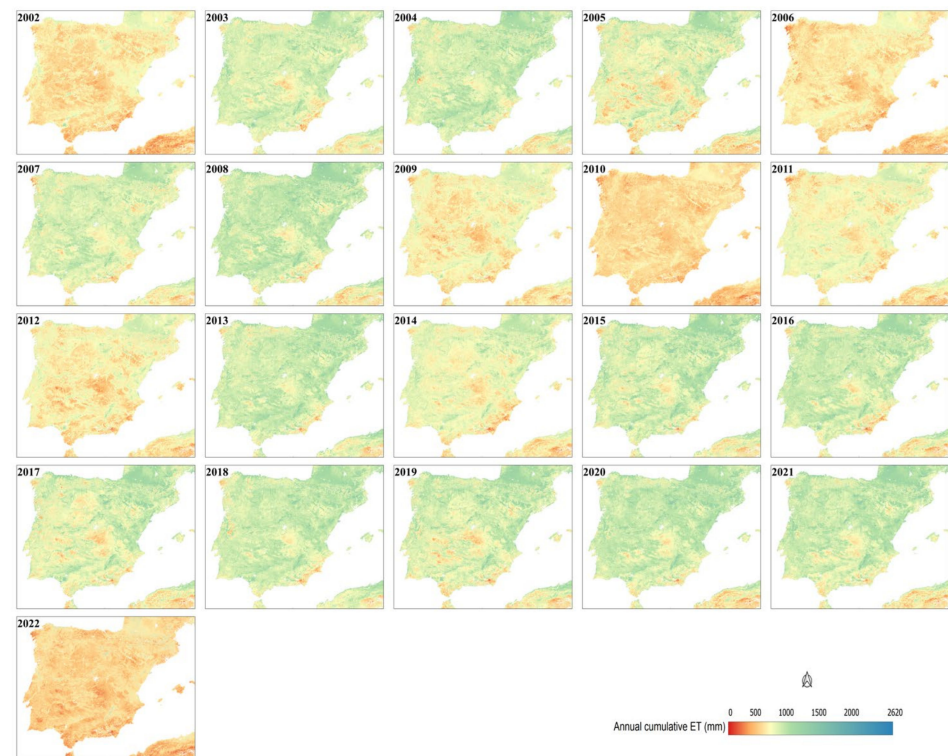
Figure 16. Spatiotemporal variability in annual cumulative of estimated ET from 2000 to 2022 in the study area using Aqua dataset.

Additionally, the figures reveal the extended duration of drought periods, particularly from 2005 to 2006 and 2009 to 2012, during which the region experienced prolonged dry conditions.

4. Discussion

4.1. Model Evaluation and Comparison with Existing Studies

In this study, the proposed modeling framework, using Terra/Aqua MODIS data, LST measurements at different viewing times, and ERA5 reanalysis data, was evaluated with 11 EC flux towers located in various land cover types (i.e., savannas, woody savannas, croplands, evergreen needleleaf forest, evergreen broadleaf forest, open shrublands). The modeled ET_d evaluated under clear-sky and all-sky observations as well as the gap-filled dataset.

The total number of clear-sky observation days (with available LST) were 5704 and 5630 for Terra and Aqua, respectively (Table 4). The model evaluation with both closed and unclosed datasets showed better performance in comparison with all-sky observations and gap-filled data (see Tables 5 and 6). These findings highlight the significant impacts of cloudy conditions on the model's performance. Cloudy conditions can alter various input variables critical to ET estimation, such as solar radiation, LST, vapor pressure, and surface emissivity [3,73], all contributing to increased errors in the model's predictions.

Additionally, the model performance was evaluated using all-sky observations, including 13,761 days for Terra and 13,329 days for Aqua, based on EC data collected from 2004 to 2020. The model showed the strongest agreement with ET_{RES}, yielding a mean RMSE of 1.53 mm·day^{-1} and 1.40 mm·day^1 for Terra and Aqua datasets, respectively. The Aqua dataset yielded the lower mean RMSE, demonstrating higher performance compared to the Terra dataset, mainly due to differences in satellite overpass times. The mean Aqua overpass time is around 13:00 solar local time, when plants are under more pronounced water stress, likely contributing to the higher performance of Aqua data in estimating ET_d (Tables 5 and 6).

After applying the gap-filling method, the total number of days compared with flux measurements increased significantly, from 13,761 to 19,265 for Terra and 13,329 to 19,265

for Aqua. However, the statistical metrics gained from comparing the gap-filled modeled ET_d with ET_{RES} showed only slight changes, with a mean RMSE of 1.85 mm·day^{-1} and 1.76 mm·day^{-1} for Terra and Aqua datasets, respectively.

The overall mean results including clear-sky and all-sky observations as well as gap-filled data with Aqua showed the lowest errors with ET_{RES}, by an MBE of 0.96 mm.day^{-1} and an average RMSE of 1.47 mm.day^{-1}, while the equivalent figures for Terra were about 1.06 mm.day^{-1} and 1.60 mm.day^{-1} (Table 7).

The gap-filling procedure showed limited effectiveness in complex systems such as FR_Pue with the IGBP classification of EBF. In contrast, the gap-filling model showed strong performance in simpler systems, like in savanna areas at the ES_LM1, ES_LM2 and ES_Abr sites. Additionally, the gap-filled data showed lower errors with the Terra dataset, indicating that the gap-filling method has limitations in estimating ET under water-stressed conditions. Overall, the mean RMSE and MBE values revealed no significant changes compared to all-sky observations, highlighting the consistency and robustness of the modeling framework. This consistency demonstrates that the gap-filling method effectively overcame missing LST data due to cloud cover yielding a spatiotemporally continuous and robust ET_d time series. Although both Terra and Aqua models overestimated ET, the intra-annual and inter-annual variability in ET in different land cover types was captured.

The modelling framework with clear-sky and all-sky observations as well as gap-filled data exhibited lower performance over forested land cover (FR_Pue). This outcome is consistent with previous studies, highlighting the limited effectiveness of the TSEB model in forested regions. Given that the TSEB model relies on turbulent transportation over croplands, the aerodynamic resistance parameterization shows a low ability in complex ecosystems such as forests [74].

Conversely, the model demonstrated higher accuracy in woody savanna and savanna areas using both clear-sky and all-sky observations, as well as gap-filled data. This result aligns with previous research, which showed smaller discrepancies between the TSEB model and ground observations in bare soil and sparsely vegetated areas [32].

The authors of [75,76] estimated ET in almond cropland using the TSEB model with Sentinel-2 and Sentinel-3 at a high spatial resolution. ET was evaluated against the soil water balance model within 148 observations, resulting in a root mean square deviation of 1.54 mm.day^{-1} and r value of 0.33. Compared to current study, in croplands (FR_Aur and FR_Lam sites), RMSE values ranged from 1.58 mm.day^{-1} to 1.87 mm.day^{-1} and r values were greater than 0.50.

The comparison of Terra/Aqua MODIS LST estimates with flux tower T_{RAD} observations (Figures 8 and 9) yielded a RMSE > 2 K and an MBE < −2 K at most of the flux stations, thus underestimating field estimates of LST, and it was particularly high in the FR_Lam site. Although these measurements did not precisely coincide with the satellite overpass times, as they were 30 min LST averages, a similar bias was found in boreal forest settings, in which LST field measurements were collected at 1 min timesteps [22]. The increase in error and bias compared to local estimates of LST using flux tower data can be attributed to several factors. These include biases in the LST due to atmospheric and emissivity corrections, sensor biases, or the unrepresentative nature of the LST at a 1 km resolution relative to the flux tower footprint. When applied regionally, the TSEB technique is typically performed in a time-differential mode as applied in this study, with the LST as one of the main input variables. Thus, the LST disagreement with field observations might have resulted in an increased bias and error in ET_d estimation, lowering the final agreement. To reduce errors caused by uncertainties in atmospheric correction and emissivity when determining the absolute LST value, an alternative time-differential TSEB technique using a dual-time difference (DTD) model in the observed LST will be implemented, adding the model refinements found in this paper and combining Terra and Aqua LST observations [34,60].

Overall, the statistical metrics in the present study indicated that the differences observed were consistent with those found in previous research on estimating ET at

regional scales. Although many of these studies only evaluated the ET accuracy over a partial annual cycle, the present study focused on estimating ET_d and evaluating the modeled ET_d with ground observations to capture the temporal year-round variability in ET in different land cover types from 2000 to 2022. For instance, [18] employed the SEB model to estimate ET_d using MODIS imagery and ground-based meteorological data. The model's results were compared with data from three EC flux towers located in native and managed grasslands over two years. The results showed that the model overestimated ET_d, with MBE and RMSE values of less than 30 $W \cdot m^{-2}$ and 50 $W \cdot m^{-2}$ (1.05 $mm \cdot day^{-1}$ and 1.75 $mm \cdot day^{-1}$, respectively). The authors of [77] utilized the evaporative fraction method with NOAA–AVHRR dataset, which has a medium spatial resolution of approximately 1 km, and the Digital Airborne Imaging Spectrometer (DAIS) dataset, which has a high spatial resolution of approximately 5 m. The ET estimations from these two datasets were compared over 13 selected dates across different land cover types. The results showed a mean RMSE of 1.4 $mm \cdot day^{-1}$. The authors of [7] presented a method for estimating continuous ET_d at a 1 km spatial resolution by integrating MODIS products and reanalysis data. To fill the gaps in LST products under cloudy conditions, a data fusion approach was applied to estimate ET using the TSEB model over croplands from 2008 to 2017. The model was validated against a total of 5707 days from five EC flux towers all located in croplands. The results showed that RMSE values range from 0.87 $mm \cdot day^{-1}$ to 1.37 $mm \cdot day^{-1}$. The authors of [78] used the Penman–Monteith model, combined with MODIS data, to estimate ET_d at 1 km spatial resolution. The model was evaluated using data from 501 days from three EC flux towers in agricultural regions (one in wheat/summer maize and the other one in orchard and maize areas), achieving a mean RMSE of 0.7 $mm \cdot day^{-1}$. The authors of [79] evaluated the accuracy of the MOD16 product, which estimates ET using the Penman–Monteith model. The ET product was validated using data from 51 days from four EC flux towers in various land cover types (vegetation, village, maize, and orchard areas). The result showed a mean RMSE of 1.2 $mm \cdot day^{-1}$. After model improvements, the RMSE dropped to 0.9 $mm \cdot day^{-1}$. The authors of [80] proposed a gap-filling method to estimate continuous ET_d using the Penman–Monteith model and remote sensing data at a 1 km spatial resolution for 2016. The model was evaluated using data from 730 days from two EC flux towers located in croplands. The results showed a mean RMSE of 0.79 $mm \cdot day^{-1}$ and 0.62 $mm \cdot day^{-1}$. Hence, unlike many studies in the literature, the present study has thoroughly evaluated the performance of the ET model across different land cover types and over long-term daily temporal scales. Accurate ET estimation approaches should also be capable of capturing the temporal variability in ET across diverse land cover types and over year-round periods to ensure robust and reliable assessments are also evaluated in this study.

Although the RMSE values from most of the flux sites align with previous studies, some flux stations exhibit lower agreement. While most correlations are statistically significant at $\alpha = 0.05$, certain flux stations showed a particularly low agreement. The authors of [7] reported similar agreement values when modeling daily ET over a long time series of MODIS data in crop areas, aligning well with the performance of certain flux stations in this study (e.g., ES_LM2, ES_LM1, ES_Abr). However, a markedly lower agreement is observed at most open shrubland flux sites, such as ES_Amo, ES_LJu, and ES_Agu. This behavior might be explained by the low ET_d variability in these sites. Averaged ET_d values of 0.43 ± 0.33, 0.44 ± 0.43, and 0.86 ± 0.58 were found for ES_Amo, ES_LJu, and ES_Agu, respectively. Although the RMSE values fall within the range reported in previous studies, these sites exhibited MBE values of 0.59, 0.17, and 1.37 $mm \cdot day^{-1}$, respectively (see Aqua results in Table 4, Model vs. Residual column), leading to greater disagreement, particularly at ES_Amo (see Figure 5). At these sites, the modeling framework failed to capture temporal dynamics. However, the high number of processed and analyzed images, combined with the heterogeneity of these surfaces and the period studies, provide consistency to the error estimates. Thus, further research will be needed at local scales using field data to enhance the model performance in these environments.

Additionally, although many flux sites selected were representative of at least one MODIS pixel, some flux sites in open shrublands, such as ES_Agu, and croplands, such as FR_Aur and FR_Lam, were relatively smaller (around 500 × 500 m). Typically, the TSEB model performs adequately in croplands. However, results yielded higher RMSE values and intermediate agreement compared to other flux sites. This may be explained by the presence of forest patches near both crop sites, which might overestimate or underestimate the LAI when the crop was active or harvested, respectively, decreasing the model agreement (see Figure 5). Finally, it is noteworthy that the ES_Cnd site showed better agreement and a similar RMSE compared to previous studies using Sentinel imagery and the Sen-ET modeling framework at a higher spatial resolution.

4.2. Application of Long Time Series of ET_d

The modeling framework applied in the study area successfully captured the spatiotemporal variation in ET within various types of land cover from 2000 to 2022.

Some past studies reported considerable drought periods within the study area over the last two decades. In connection with these studies, changes observed in the intra-annual and inter-annual timescale of the estimated ET_d align with the drought events documented [48,76].

The annual cumulative ET underwent a significant reduction in 2005 in all sites except for the FR_Aur and FR_Lam sites with both Terra and Aqua datasets. Ref. [47] utilized the Standardized Precipitation Index (SPI) and the Standardized Precipitation–Evapotranspiration Index (SPEI) to identify drought events in the IP from 1961 to 2011, noting 2005 as one of the major drought events in this study area. Additionally, [48] characterized drought events across the IP using the SPI from 1916 to 2020, identifying 2005 as having notable drought periods.

In the northern (FR_Aur and FR_Lam sites) and southeastern (ES_Amo and ES_Agu sites) parts of the study area, there were remarkable reductions in the growing seasons (Figures 12 and 13) and annual cumulative ET (Figure 14) in 2003. In addition, the outliers beyond the lower fence (Figures 10 and 11) observed in the FR_Lam and FR_Aur sites in May and August 2003 are associated with the significant ET changes in this area. [81] analyzed soil moisture during the 2003 drought event in Europe and indicated that 2003 was a significant drought event in the Euro-Mediterranean region.

Notably, there is a declining trend in the ET time series across all sites in 2022 (Figure 14). Ref. [82] demonstrated that the Euro-Mediterranean region was under severe drought conditions in 2022. Figures 10 and 11 show outliers beyond the lower fence at the ES_Pue site in July 2022, illustrating abnormal changes in the ET time series that were also captured by the modeling framework.

In the southeastern part of the study area (OSH sites), the minimum annual cumulative ET values were recorded in 2005, indicating significant water stress on vegetation (Figure 14). This finding aligns with [83], which used the SPI to monitor drought in this region. The result demonstrated that the southeastern part of the study area experienced a significant drought in 2005. For both Terra and Aqua datasets, outliers beyond the lower fence at the ES_LgS site (Figures 10 and 11) were observed in May, September, and March in 2005, 2012, and 2017, respectively, also aligning with [48], which reported drought events.

The annual cumulative ET values at sites located in savanna and woody savanna areas (ES_LM1, ES_LM2, ES_Abr, ES_Cnd) showed less fluctuation over the time series, with notable reductions in 2005 and 2012 (Figure 14). This result agrees with [84,85], which reported 2005 as the driest year in the Guandiana River basin. Additionally, the annual cumulative ET experienced significant reductions at the ES_LM1, ES_LM2 and ES_Abr sites in 2009, and at the ES_Abr site in 2019, aligning with the findings of [48]. In Figures 10 and 11, outliers beyond the lower fence observed at savanna sites during the growing seasons in 2009 and 2012 indicate unexpected changes in the ET time series, corresponding with drought years in this area reported by [46,48]. Moreover, outliers beyond the lower fence were observed in 2005 and 2012 at the ES_Cnd site from February to July.

This research highlights that the study areas experienced significant water stress from 2000 to 2022, varying across the regions (Figures 15 and 16). This underscores the critical importance of monitoring ET to recognize vegetation water stress and drought, as evidenced by significant changes in the ET time series. In addition, the ET trends suggest that future droughts could exacerbate water scarcity in these vulnerable areas. This pattern could have implications for food security and ecosystem health in the region.

4.3. Limitations of the Proposed Modelling Framework and Future Implementation

Without any site-specific adjustments and relying only on global datasets, the modeling framework produced ET_d estimates comparable to those reported in other studies in terms of error, demonstrating robustness across various land cover types. However, agreement at certain flux sites could be increased by improving some of the input variables.

Similarly to other studies, the model accuracy and agreement could be improved by using more accurate meteorological data (especially wind speed measurements). As [24,37] suggested, atmospheric forces from numerical weather prediction models may introduce some uncertainty to the TSEB model compared to using local meteorological data. Several studies [7,24] have relied on ERA5 reanalysis data to estimate ET. Despite the low spatial resolution of ERA5 (approximately 35 km), comparisons with meteorological instruments at several flux sites have shown strong agreement for most key meteorological parameters, except for wind speed and solar radiation. This discrepancy may directly affect the accuracy of the TSEB model in estimating Rn and, consequently, ET, since ET is calculated as a residual of the energy balance. Therefore, errors in ET_d could be significantly reduced if more accurate solar radiation inputs were used, especially in temperate areas (i.e., radiation-limited) which are more sensitive to uncertainty in available energy[37]. Additionally, errors in both air temperature and wind speed primarily affect the retrievals of the sensible heat flux, which is more critical in the estimation of LE in semi-arid (i.e., water-limited) areas [37].

To address these issues, an alternative climate forcing dataset such as ERA-Land, with an improved spatial resolution of approximately 9 km, could be used as TSEB meteorological input. However, the primary drawback is that the ERA-Land product applies a land mask, potentially excluding a 9 km area in regions near the seashore, rendering the modeling framework inapplicable in those areas. Additionally, there is no available layer for wind speed. For solar radiation, other methodologies or products could be utilized. The authors of [86] proposed a DEM-based hybrid methodology, which has been successfully used to estimate Rn at daily scales [87] and can also be useful for ET daily upscaling. Other current solar radiation products, such as the MSG-SAF solar radiation product, have demonstrated accurate evaluation results with in situ measurements, proving to be an effective input for calculating evaporative fluxes [88].

Finally, values for H_c and Ω in Table 3 were meant to fit a global-based land cover legend and can significantly deviate from the actual values at specific flux sites. Thus, utilizing ancillary remote sensing-based products derived from LiDAR data [89] would increase the accuracy of surface characteristic parameterizations.

5. Conclusions

Estimating ET at regional scales with daily temporal resolution can benefit drought monitoring in water-limited regions. Global ET datasets often lack a daily temporal resolution with a finer spatial scale. This research addresses these gaps by providing spatiotemporally continuous ET data, offering a significant advancement over existing ET products in this region. A modeling framework, based on the SEN-ET scheme, was used with Terra/Aqua MODIS data and the ERA5 atmospheric reanalysis dataset to estimate ET across various land cover types (i.e., savannas, woody savannas, croplands, evergreen broadleaf forest, open shrublands) from 2000 to 2022. The main conclusions are as follows:

1. The modeling framework was evaluated with clear-sky and all-sky observations as well as gap-filled data. Under clear-sky observations, the model demonstrated lower

errors and higher correlations with both closed and unclosed datasets compared to all-sky observations and gap-filled data. These findings highlighted the negative impact of cloudy conditions on the model's performance. Moreover, the overall mean results, including clear-sky and all-sky observations as well as gap-filled data with the Aqua dataset, showed the lowest errors against ET_{RES}, by an MBE of 0.96 mm.day^{-1}, an average RMSE of 1.47 mm.day^{-1}, and r value of 0.51. The equivalent figures for the Terra dataset were about 1.06 mm.day^{-1}, 1.60 mm.day^{-1}, and 0.52. The Aqua dataset showed better performance compared to the Terra dataset, primarily due to differences in satellite overpass times and a smaller MBE between Aqua LST products and in situ LST measurements. The overestimation errors obtained in this study were within the range of errors observed in previous studies that estimated ET at regional scales. Importantly, the model was able to capture both intra-annual and inter-annual variability in ET in different land cover types. By successfully gap-filling cloudy or low-quality satellite observations, the model achieved more comprehensive spatiotemporal coverage, solving a major limitation in consistent ET monitoring. Furthermore, the performance metrics (RMSE and MBE) remained consistent after applying gap-filling methods, further underscoring the robustness and reliability of the model's ET estimations. However, for some flux stations, a low agreement but statistically significant correlation was found. Thus, further modelling framework and TSEB adjustments will be needed to improve the modelling results, such as using more accurate solar radiation products and climate forcing data. Moreover, some local TSEB mode evaluations, especially in semi-arid open shrublands, will be also needed.

2. The alignment between the spatiotemporal trends in the estimated ET time series and documented drought events underscores the reliability of ET as a robust indicator for drought monitoring. The modeling framework's ability to reflect changes in ET in response to water stress and drought conditions highlights its potential for improving water resource management at regional scales. The findings suggest that the ET data generated from this modeling framework can serve as a valuable tool for drought early warning systems.

Author Contributions: Conceptualization, M.B. and J.C.; methodology, M.B. and J.C.; software, M.B. and J.C.; data curation, M.B., J.C., and M.P.-S.; writing, review, and editing, M.B., J.C. and M.P.-S.; graphical deployment, M.B.; supervision, J.C. All authors have read and agreed to the published version of the manuscript.

Data Availability Statement: Restrictions apply to the datasets. The datasets presented in this article are not readily available because the data are part of an ongoing study. Requests to access the datasets should be directed to Jordi Cristóbal (jordi.cristóbal@uab.cat).

Conflicts of Interest: The authors declare no conflicts of interest.

Appendix A. Summary of Equations Used to Estimate Aerodynamic Resistances in TSEB

In this appendix, the resistances involved in Equations (5)–(7) are summarized [28]. R_A is the aerodynamic resistance in the surface layer computed from the stability-corrected temperature profile equations (s·m^{-1}), defined as follows:

$$R_A = \frac{([In((z_U - d_0)/z_{0M}) - \Psi_M][In((z_T - d_0)/z_{0H}] - \Psi_H)]}{k^2 u} \tag{A1}$$

where d_O is the displacement height, U is the wind speed measured at height z_U, k is von Karman's constant (≈ 0.4), z_T is the height of the T_A measurement, Ψ_M and Ψ_H are the Monin–Obukhov stability functions for momentum and heat, respectively, and z_{OM} is the aerodynamic roughness length. Both d_O and z_{OM} were estimated using the LAI and canopy height (H_C, see Table 3) as follows [90,91]:

$$d_O = 0.7 - \left(\frac{1}{(5n)\left(1 - e^{(-3.3n)}\right)} \right) H_C \tag{A2}$$

where n is the within-canopy wind speed profile extinction coefficient, parameterized as follows:

$$n = \frac{C_d\, LAI}{2\left(\frac{u_*}{u(h)}\right)^2} \tag{A3}$$

where *Cd* is the drag coefficient of the foliage elements with a value of 0.2, and the ratio $u_*/u(h)$ is parameterized as follows:

$$\frac{u_*}{u(h)} = 0.360 - 0.264\, e^{(-15.1 * C_d * LAI)} \tag{A4}$$

Finally, z_{OM} is defined as follows:

$$z_{OM} = (1 - d_O)e^{-0.4\,/\,\frac{u_*}{u(h)}}\, Hc \tag{A5}$$

R_S is the resistance to the heat flow in the boundary layer above the soil (s·m^{-1}), defined as follows:

$$R_S = \frac{1}{a\prime + b\prime U_S} \tag{A6}$$

where a' ≈ 0.004 m·s^{-1}, a' ≈ 0.012 m·s^{-1}, U_S is the wind speed (m·s^{-1}) at the height above the soil surface where the effect of the soil surface roughness is minimal (~5 cm) and estimated from the [82] wind attenuation model through the canopy layer (see Equation (A8)).

Finally, R_X is the total boundary layer resistance of the vegetation leaf layer (s·m^{-1}), defined as follows:

$$R_X = \frac{C'}{LAI}\left(\frac{S}{U_{d_o+Z_{om}}} \right)^{\frac{1}{2}} \tag{A7}$$

where C' is derived from weighting a coefficient in the equation for the leaf boundary layer resistance (assumed a constant ~90 s$^{1/2}$ m^{-1}) and S is the leaf size (m). U_{d+Zm} is given by the following:

$$U_{d_o+Z_{om}} = U_C\, exp\left[-a\left(1 - \frac{d_o + Z_{om}}{H_C} \right) \right] \tag{A8}$$

where U_C is the wind speed at the canopy height (Hc) and *a* is the wind attenuation coefficient of the [82] wind attenuation model, which is a function of the LAI, Hc, and leaf size. For a full description of the TSEB resistance formulations, see [27–29].

References

1. IPCC. IPCC Synthesis Report—Climate Change 2023. In *An Assessment of the Intergovernmental Panel on Climate Change*; IPPC: Geneva, Switzerland, 2022; Volume 335.
2. Noto, L.V.; Cipolla, G.; Pumo, D.; Francipane, A. Climate Change in the Mediterranean Basin (Part II): A Review of Challenges and Uncertainties in Climate Change Modeling and Impact Analyses. *Water Resour. Manag.* **2023**, *37*, 2307–2323. [CrossRef]
3. Wang, K.; Dickinson, R.E. A Review of Global Terrestrial Evapotranspiration: Observation, Modeling, Climatology, and Climatic Variability. *Rev. Geophys.* **2012**, *50*, RG2005. [CrossRef]
4. Jung, M.; Reichstein, M.; Ciais, P.; Seneviratne, S.I.; Sheffield, J.; Goulden, M.L.; Bonan, G.; Cescatti, A.; Chen, J.; de Jeu, R.; et al. Recent Decline in the Global Land Evapotranspiration Trend Due to Limited Moisture Supply. *Nature* **2010**, *467*, 951–954. [CrossRef]

5. Kimball, B.A.; Thorp, K.R.; Boote, K.J.; Stockle, C.; Suyker, A.E.; Evett, S.R.; Brauer, D.K.; Coyle, G.G.; Copeland, K.S.; Marek, G.W.; et al. Simulation of Evapotranspiration and Yield of Maize: An Inter-Comparison among 41 Maize Models. *Agric. For. Meteorol.* **2023**, *333*, 109396. [CrossRef]

6. Ma, Y.; Liu, S.; Song, L.; Xu, Z.; Liu, Y.; Xu, T.; Zhu, Z. Estimation of Daily Evapotranspiration and Irrigation Water Efficiency at a Landsat-like Scale for an Arid Irrigation Area Using Multi-Source Remote Sensing Data. *Remote Sens. Environ.* **2018**, *216*, 715–734. [CrossRef]

7. Zhang, C.; Long, D.; Zhang, Y.; Anderson, M.C.; Kustas, W.P.; Yang, Y. A Decadal (2008–2017) Daily Evapotranspiration Data Set of 1 Km Spatial Resolution and Spatial Completeness across the North China Plain Using TSEB and Data Fusion. *Remote Sens. Environ.* **2021**, *262*, 112519. [CrossRef]

8. Allen, R.G.; Pereira, L.S.; Raes, D.; Smith, M. *Crop Evapotranspiration—Guidelines for Computing Crop Water Requirements—FAO Irrigation and Drainage Paper 56*; Food and Agriculture Organization of the United Nations: Rome, Italy, 1998.

9. Stoyanova, J.S.; Georgiev, C.G.; Neytchev, P.N. Drought Monitoring in Terms of Evapotranspiration Based on Satellite Data from Meteosat in Areas of Strong Land–Atmosphere Coupling. *Land* **2023**, *12*, 240. [CrossRef]

10. Liu, J.; You, Y.; Li, J.; Sitch, S.; Gu, X.; Nabel, J.E.M.S.; Lombardozzi, D.; Luo, M.; Feng, X.; Arneth, A.; et al. Response of Global Land Evapotranspiration to Climate Change, Elevated CO_2, and Land Use Change. *Agric. For. Meteorol.* **2021**, *311*, 108663. [CrossRef]

11. Pendergrass, A.G.; Meehl, G.A.; Pulwarty, R.; Hobbins, M.; Hoell, A.; AghaKouchak, A.; Bonfils, C.J.W.; Gallant, A.J.E.; Hoerling, M.; Hoffmann, D.; et al. Flash Droughts Present a New Challenge for Subseasonal-to-Seasonal Prediction. *Nat. Clim. Chang.* **2020**, *10*, 191–199. [CrossRef]

12. Howell, T.A.; Schneider, A.D.; Jensen, M.E. History of Lysimeter Design and Use for Evapotranspiration Measurements. In Proceedings of the Lysimeters for Evapotranspiration and Environmental Measurements, Honolulu, HI, USA, 23–25 July 1991.

13. Bernhofer, C. Estimating Forest Evapotranspiration at a Non-Ideal Site. *Agric. For. Meteorol.* **1992**, *60*, 17–32. [CrossRef]

14. Ding, R.; Kang, S.; Li, F.; Zhang, Y.; Tong, L.; Sun, Q. Evaluating Eddy Covariance Method by Large-Scale Weighing Lysimeter in a Maize Field of Northwest China. *Agric. Water Manag.* **2010**, *98*, 87–95. [CrossRef]

15. Ma, N.; Szilagyi, J.; Zhang, Y. Calibration-Free Complementary Relationship Estimates Terrestrial Evapotranspiration Globally. *Water Resour. Res.* **2021**, *57*, e2021WR029691. [CrossRef]

16. Khorrami, B.; Gorjifard, S.; Ali, S.; Feizizadeh, B. Local-Scale Monitoring of Evapotranspiration Based on Downscaled GRACE Observations and Remotely Sensed Data: An Application of Terrestrial Water Balance Approach. *Earth Sci. Inform.* **2023**, *16*, 1329–1345. [CrossRef]

17. Ramos, J.G.; Cratchley, C.R.; Kay, J.A.; Casterad, M.A.; Martínez-Cob, A.; Domínguez, R. Evaluation of Satellite Evapotranspiration Estimates Using Ground-Meteorological Data Available for the Flumen District into the Ebro Valley of N.E. Spain. *Agric. Water Manag.* **2009**, *96*, 638–652. [CrossRef]

18. Khand, K.; Taghvaeian, S.; Gowda, P.; Paul, G. A Modeling Framework for Deriving Daily Time Series of Evapotranspiration Maps Using a Surface Energy Balance Model. *Remote Sens.* **2019**, *11*, 508. [CrossRef]

19. Kalma, J.D.; McVicar, T.R.; McCabe, M.F. Estimating Land Surface Evaporation: A Review of Methods Using Remotely Sensed Surface Temperature Data. *Surv. Geophys.* **2008**, *29*, 421–469. [CrossRef]

20. Andreu, A.; Kustas, W.P.; Polo, M.J.; Carrara, A.; González-Dugo, M.P. Modeling Surface Energy Fluxes over a Dehesa (Oak Savanna) Ecosystem Using a Thermal Based Two-Source Energy Balance Model (TSEB) I. *Remote Sens.* **2018**, *10*, 567. [CrossRef]

21. Comini de Andrade, B.; Laipelt, L.; Fleischmann, A.; Huntington, J.; Morton, C.; Melton, F.; Erickson, T.; Roberti, D.R.; de Arruda Souza, V.; Biudes, M.; et al. GeeSEBAL-MODIS: Continental-Scale Evapotranspiration Based on the Surface Energy Balance for South America. *ISPRS J. Photogramm. Remote Sens.* **2024**, *207*, 141–163. [CrossRef]

22. Cristóbal, J.; Prakash, A.; Anderson, M.C.; Kustas, W.P.; Alfieri, J.G.; Gens, R. Surface Energy Flux Estimation in Two Boreal Settings in Alaska Using a Thermal-Based Remote Sensing Model. *Remote Sens.* **2020**, *12*, 4108. [CrossRef]

23. Bozorgi, M.; Cristóbal, J. An Integrated Modelling Framework to Estimate Time Series of Evapotranspiration at Regional Scales Using MODIS Data and a Two-Source Energy Balance Model. In Proceedings of the the 5th International Electronic Conference on Remote Sensing, Online, 7–21 November 2023; MDPI: Basel, Switzerland, 2023.

24. Aguirre-García, S.D.; Aranda-Barranco, S.; Nieto, H.; Serrano-Ortiz, P.; Sánchez-Cañete, E.P.; Guerrero-Rascado, J.L. Modelling Actual Evapotranspiration Using a Two Source Energy Balance Model with Sentinel Imagery in Herbaceous-Free and Herbaceous-Cover Mediterranean Olive Orchards. *Agric. For. Meteorol.* **2021**, *311*, 108692. [CrossRef]

25. Kustas, W.; Anderson, M. Advances in Thermal Infrared Remote Sensing for Land Surface Modeling. *Agric. For. Meteorol.* **2009**, *149*, 2071–2081. [CrossRef]

26. Anderson, M.C.; Kustas, W.P.; Norman, J.M.; Diak, G.T.; Hain, C.R.; Gao, F.; Yang, Y.; Knipper, K.R.; Xue, J.; Yang, Y.; et al. A Brief History of the Thermal IR-Based Two-Source Energy Balance (TSEB) Model—Diagnosing Evapotranspiration from Plant to Global Scales. *Agric. For. Meteorol.* **2024**, *350*, 109951. [CrossRef]

27. Kustas, W.P.; Norman, J.M. Evaluation of Soil and Vegetation Heat Flux Predictions Using a Simple Two-Source Model with Radiometric Temperatures for Partial Canopy Cover. *Agric. For. Meteorol.* **1999**, *94*, 13–29. [CrossRef]

28. Norman, J.M.; Kustas, W.P.; Humes, K.S. Source Approach for Estimating Soil and Vegetation Energy Fluxes in Observations of Directional Radiometric Surface Temperature. *Agric. For. Meteorol.* **1995**, *77*, 263–293. [CrossRef]

29. Kustas, W.P.; Norman, J.M. A Two-Source Energy Balance Approach Using Directional Radiometric Temperature Observations for Sparse Canopy Covered Surfaces. *Agron. J.* **2000**, *92*, 847–854. [CrossRef]

30. Bastiaanssen, W.G.M.; Menenti, M.; Feddes, R.A.; Holtslag, A.A.M. A Remote Sensing Surface Energy Balance Algorithm for Land (SEBAL): 1. Formulation. *J. Hydrol.* **1998**, *212–213*, 198–212. [CrossRef]

31. Allen, R.G.; Tasumi, M.; Trezza, R. Satellite-Based Energy Balance for Mapping Evapotranspiration with Internalized Calibration (METRIC)—Model. *J. Irrig. Drain. Eng.* **2007**, *133*, 380–394. [CrossRef]

32. Timmermans, W.J.; Kustas, W.P.; Anderson, M.C.; French, A.N. An Intercomparison of the Surface Energy Balance Algorithm for Land (SEBAL) and the Two-Source Energy Balance (TSEB) Modeling Schemes. *Remote Sens. Environ.* **2007**, *108*, 369–384. [CrossRef]

33. Norman, J.M.; Anderson, M.C.; Kustas, W.P.; French, A.N.; Mecikalski, J.; Torn, R.; Diak, G.R.; Schmugge, T.J.; Tanner, B.C.W. Remote Sensing of Surface Energy Fluxes at 101-m Pixel Resolutions. *Water Resour. Res.* **2003**, *39*, 1775. [CrossRef]

34. Guzinski, R.; Anderson, M.C.; Kustas, W.P.; Nieto, H.; Sandholt, I. Using a Thermal-Based Two Source Energy Balance Model with Time-Differencing to Estimate Surface Energy Fluxes with Day-Night MODIS Observations. *Hydrol. Earth Syst. Sci.* **2013**, *17*, 2809–2825. [CrossRef]

35. Kustas, W.P.; Bindlish, R.; French, A.N.; Schmugge, T.J. Comparison of Energy Balance Modeling Schemes Using Microwave-Derived Soil Moisture and Radiometric Surface Temperature. *Water Resour. Res.* **2003**, *39*, 1039. [CrossRef]

36. Anderson, M.C.; Norman, J.M.; Diak, G.R.; Kustas, W.P.; Mecikalski, J.R. A Two-Source Time-Integrated Model for Estimating Surface Fluxes Using Thermal Infrared Remote Sensing. *Remote Sens. Environ.* **1997**, *60*, 195–216. [CrossRef]

37. Guzinski, R.; Nieto, H.; Sandholt, I.; Karamitilios, G. Modelling High-Resolution Actual Evapotranspiration through Sentinel-2 and Sentinel-3 Data Fusion. *Remote Sens.* **2020**, *12*, 1433. [CrossRef]

38. Xu, T.; Guo, Z.; Xia, Y.; Ferreira, V.G.; Liu, S.; Wang, K.; Yao, Y.; Zhang, X.; Zhao, C. Evaluation of Twelve Evapotranspiration Products from Machine Learning, Remote Sensing and Land Surface Models over Conterminous United States. *J. Hydrol.* **2019**, *578*, 124105. [CrossRef]

39. Martens, B.; Miralles, D.G.; Lievens, H.; Van Der Schalie, R.; De Jeu, R.A.M.; Fernández-Prieto, D.; Beck, H.E.; Dorigo, W.A.; Verhoest, N.E.C. GLEAM v3: Satellite-Based Land Evaporation and Root-Zone Soil Moisture. *Geosci. Model Dev.* **2017**, *10*, 1903–1925. [CrossRef]

40. Senay, G.B.; Bohms, S.; Singh, R.K.; Gowda, P.H.; Velpuri, N.M.; Alemu, H.; Verdin, J.P. Operational Evapotranspiration Mapping Using Remote Sensing and Weather Datasets: A New Parameterization for the SSEB Approach. *J. Am. Water Resour. Assoc.* **2013**, *49*, 577–591. [CrossRef]

41. Mu, Q.; Zhao, M.; Running, S.W. Improvements to a MODIS Global Terrestrial Evapotranspiration Algorithm. *Remote Sens. Environ.* **2011**, *115*, 1781–1800. [CrossRef]

42. Yao, Y.; Liang, S.; Li, X.; Hong, Y.; Fisher, J.B.; Zhang, N.; Chen, J.; Cheng, J.; Zhao, S.; Zhang, X.; et al. Bayesian Multimodel Estimation of Global Terrestrial Latent Heat Flux from Eddy Covariance, Meteorological, and Satellite Observations. *J. Geophys. Res.* **2014**, *119*, 4521–4545. [CrossRef]

43. Bellvert, J.; Jofre-Ĉekalović, C.; Pelechá, A.; Mata, M.; Nieto, H. Feasibility of Using the Two-Source Energy Balance Model (TSEB) with Sentinel-2 and Sentinel-3 Images to Analyze the Spatio-Temporal Variability of Vine Water Status in a Vineyard. *Remote Sens.* **2020**, *12*, 2299. [CrossRef]

44. Possega, M.; García-Valdecasas Ojeda, M.; Gámiz-Fortis, S.R. Multi-Scale Analysis of Agricultural Drought Propagation on the Iberian Peninsula Using Non-Parametric Indices. *Water* **2023**, *15*, 2032. [CrossRef]

45. Almendra-Martín, L.; Martínez-Fernández, J.; González-Zamora, Á.; Benito-Verdugo, P.; Herrero-Jiménez, C.M. Agricultural Drought Trends on the Iberian Peninsula: An Analysis Using Modeled and Reanalysis Soil Moisture Products. *Atmosphere* **2021**, *12*, 236. [CrossRef]

46. Páscoa, P.; Gouveia, C.M.; Russo, A.; Trigo, R.M. Drought Trends in the Iberian Peninsula over the Last 112 Years. *Adv. Meteorol.* **2017**, *2017*, 4653126. [CrossRef]

47. Vicente-Serrano, S.M.; Lopez-Moreno, J.I.; Beguería, S.; Lorenzo-Lacruz, J.; Sanchez-Lorenzo, A.; García-Ruiz, J.M.; Azorin-Molina, C.; Morán-Tejeda, E.; Revuelto, J.; Trigo, R.; et al. Evidence of Increasing Drought Severity Caused by Temperature Rise in Southern Europe. *Environ. Res. Lett.* **2014**, *9*, 044001. [CrossRef]

48. Trullenque-Blanco, V.; Beguería, S.; Vicente-Serrano, S.M.; Peña-Angulo, D.; González-Hidalgo, C. Catalogue of Drought Events in Peninsular Spanish along 1916–2020 Period. *Sci. Data* **2024**, *11*, 703. [CrossRef]

49. Wilson, K.; Goldstein, A.; Falge, E.; Aubinet, M.; Baldocchi, D.; Berbigier, P.; Bernhofer, C.; Ceulemans, R.; Dolman, H.; Field, C.; et al. Energy Balance Closure at FLUXNET Sites. *Agric. For. Meteorol.* **2002**, *113*, 223–243. [CrossRef]

50. Jin, Y.; Liu, Y.; Liu, J.; Zhang, X. Energy Balance Closure Problem over a Tropical Seasonal Rainforest in Xishuangbanna, Southwest China: Role of Latent Heat Flux. *Water* **2022**, *14*, 395. [CrossRef]

51. McGloin, R.; Šigut, L.; Havránková, K.; Dušek, J.; Pavelka, M.; Sedlák, P. Energy Balance Closure at a Variety of Ecosystems in Central Europe with Contrasting Topographies. *Agric. For. Meteorol.* **2018**, *248*, 418–431. [CrossRef]

52. Stoy, P.C.; Mauder, M.; Foken, T.; Marcolla, B.; Boegh, E.; Ibrom, A.; Arain, M.A.; Arneth, A.; Aurela, M.; Bernhofer, C.; et al. A Data-Driven Analysis of Energy Balance Closure across FLUXNET Research Sites: The Role of Landscape Scale Heterogeneity. *Agric. For. Meteorol.* **2013**, *171–172*, 137–152. [CrossRef]

53. Twine, T.E.; Kustas, W.P.; Norman, J.M.; Cook, D.R.; Houser, P.R.; Meyers, T.P.; Prueger, J.H.; Starks, P.J.; Wesely, M.L. Correcting Eddy-Covariance Flux Underestimates over a Grassland. *Agric. For. Meteorol.* **2000**, *103*, 279–300. [CrossRef]

54. Foken, T. The Energy Balance Closure Problem: An Overview. *Ecol. Appl.* **2008**, *18*, 1351–1367. [CrossRef] [PubMed]

55. Li, F.; Kustas, W.P.; Anderson, M.C.; Prueger, J.H.; Scott, R.L. Effect of Remote Sensing Spatial Resolution on Interpreting Tower-Based Flux Observations. *Remote Sens. Environ.* **2008**, *112*, 337–349. [CrossRef]

56. Jiang, Y.; Tang, R.; Jiang, X.; Li, Z.L. Impact of Clouds on the Estimation of Daily Evapotranspiration from MODIS-Derived Instantaneous Evapotranspiration Using the Constant Global Shortwave Radiation Ratio Method. *Int. J. Remote Sens.* **2019**, *40*, 1930–1944. [CrossRef]

57. Gao, F.; Morisette, J.T.; Wolfe, R.E.; Ederer, G.; Pedelty, J.; Masuoka, E.; Myneni, R.; Tan, B.; Nightingale, J. An Algorithm to Produce Temporally and Spatially Continuous MODIS-LAI Time Series. *IEEE Geosci. Remote Sens. Lett.* **2008**, *5*, 60–64. [CrossRef]

58. Aguilar, C.; Herrero, J.; Polo, M.J. Topographic Effects on Solar Radiation Distribution in Mountainous Watersheds and Their Influence on Reference Evapotranspiration Estimates at Watershed Scale. *Hydrol. Earth Syst. Sci.* **2010**, *14*, 2479–2494. [CrossRef]

59. Norman, J.M.; Becker, F. Terminology in Thermal Infrared Remote Sensing of Natural Surfaces. *Agric. For. Meteorol.* **1995**, *77*, 153–166. [CrossRef]

60. Norman, J.M.; Kustas, W.P.; Prueger, J.H.; Diak, G.R. Surface Flux Estimation Using Radiometric Temperature: A Dual-Temperatare-Difference Method to Minimize Measurement Errors. *Water Resour. Res.* **2000**, *36*, 2263–2274. [CrossRef]

61. Kustas, W.P.; Anderson, M.C.; Alfieri, J.G.; Knipppper, K.; Torres-Rua, A.; Parry, C.K.; Nieto, H.; Agam, N.; White, W.A.; Gao, F.; et al. The Grape Remote Sensing Atmospheric Profile and Evapotranspiration Experiment. *Bull. Am. Meteorol. Soc.* **2018**, *99*, 1791–1812. [CrossRef]

62. Brutsaert, W. On a Derivable Formula for Long-wave Radiation from Clear Skies. *Water Resour. Res.* **1975**, *11*, 742–744. [CrossRef]

63. Choudhury, B.J.; Idso, S.B.; Reginato, R.J. Analysis of an Empirical Model for Soil Heat Flux under a Growing Wheat Crop for Estimating Evaporation by an Infrared-Temperature Based Energy Balance Equation. *Agric. For. Meteorol.* **1987**, *39*, 283–297. [CrossRef]

64. Priestley, C.H.B.; Taylor, R.J. On the Assessment of Surface Heat Flux and Evaporation Using Large-Scale Parameters. *Mon. Weather. Rev.* **1972**, *100*, 81–92. [CrossRef]

65. Tanner, C.B.; Jury, W.A. Estimating Evaporation and Transpiration from a Row Crop during Incomplete Cover 1. *Agron. J.* **1976**, *68*, 239–243. [CrossRef]

66. Fisher, J.B.; Tu, K.P.; Baldocchi, D.D. Global Estimates of the Land-Atmosphere Water Flux Based on Monthly AVHRR and ISLSCP-II Data, Validated at 16 FLUXNET Sites. *Remote Sens. Environ.* **2008**, *112*, 901–919. [CrossRef]

67. Anderson, M.C.; Norman, J.M.; Kustas, W.P.; Li, F.; Prueger, J.H.; Mecikalski, J.R. Effects of Vegetation Clumping on Two-Source Model Estimates of Surface Energy Fluxes from an Agricultural Landscape during SMACEX. *J. Hydrometeorol.* **2005**, *6*, 892–909. [CrossRef]

68. Li, F.; Kustas, W.P.; Prueger, J.H.; Neale, C.M.U.; Jackson, T.J. Utility of Remote-Sensing-Based Two-Source Energy Balance Model under Low- and High-Vegetation Cover Conditions. *J. Hydrometeorol.* **2005**, *6*, 878–891. [CrossRef]

69. Guzinski, R.; Nieto, H.; Sanchez, J.M.; Lopez-Urrea, R.; Boujnah, D.M.; Boulet, G. Utility of Copernicus-Based Inputs for Actual Evapotranspiration Modeling in Support of Sustainable Water Use in Agriculture. *IEEE J. Sel. Top. Appl. Earth Obs. Remote Sens.* **2021**, *14*, 11466–11484. [CrossRef]

70. Wan, Z.; Li, Z.L. A Physics-Based Algorithm for Retrieving Land-Surface Emissivity and Temperature from Eos/Modis Data. *IEEE Trans. Geosci. Remote Sens.* **1997**, *35*, 980–996. [CrossRef]

71. Kustas, W.P.; Nieto, H.; Morillas, L.; Anderson, M.C.; Alfieri, J.G.; Hipps, L.E.; Villagarcía, L.; Domingo, F.; Garcia, M. Revisiting the Paper "Using Radiometric Surface Temperature for Surface Energy Flux Estimation in Mediterranean Drylands from a Two-Source Perspective". *Remote Sens. Environ.* **2016**, *184*, 645–653. [CrossRef]

72. Semmens, K.A.; Anderson, M.C.; Kustas, W.P.; Gao, F.; Alfieri, J.G.; McKee, L.; Prueger, J.H.; Hain, C.R.; Cammalleri, C.; Yang, Y.; et al. Monitoring Daily Evapotranspiration over Two California Vineyards Using Landsat 8 in a Multi-Sensor Data Fusion Approach. *Remote Sens. Environ.* **2016**, *185*, 155–170. [CrossRef]

73. Roderick, M.L.; Farquhar, G.D. The Cause of Decreased Pan Evaporation over the Past 50 Years. *Science* **2002**, *298*, 1410–1411. [CrossRef]

74. Sun, L.; Liang, S.; Chen, Z. Comparison of et Models over Different Land Cover. *IOP Conf. Ser. Earth Environ. Sci.* **2024**, *17*, 012128. [CrossRef]

75. Jofre-Cekalovic, C.; Nieto, H.; Girona, J.; Pamies-Sans, M.; Bellvert, J. Accounting for Almond CropWater Use under Different Irrigation Regimes with a Two-Source Energy Balance Model and Copernicus-Based Inputs. *Remote Sens.* **2022**, *14*, 2106. [CrossRef]

76. Páscoa, P.; Russo, A.; Gouveia, C.M.; Soares, P.M.M.; Cardoso, R.M.; Careto, J.A.M.; Ribeiro, A.F.S. A High-Resolution View of the Recent Drought Trends over the Iberian Peninsula. *Weather. Clim. Extrem.* **2021**, *32*, 100320. [CrossRef]

77. Sobrino, J.A.; Gómez, M.; Jiménez-Muñoz, J.C.; Olioso, A. Application of a Simple Algorithm to Estimate Daily Evapotranspiration from NOAA-AVHRR Images for the Iberian Peninsula. *Remote Sens. Environ.* **2007**, *110*, 139–148. [CrossRef]

78. Hu, X.; Shi, L.; Lin, L.; Zhang, B.; Zha, Y. Optical-Based and Thermal-Based Surface Conductance and Actual Evapotranspiration Estimation, an Evaluation Study in the North China Plain. *Agric. For. Meteorol.* **2018**, *263*, 449–464. [CrossRef]

79. Liu, S.; Han, Y.; Su, H. Regional Evapotranspiration Estimation by the Improved MOD16-Sm Model and Its Application in Central China. *Water* **2022**, *14*, 1491. [CrossRef]

80. Xu, J.; Wu, B.; Yan, N.; Tan, S. Regional Daily ET Estimates Based on the Gap-Filling Method of Surface Conductance. *Remote Sens.* **2018**, *10*, 554. [CrossRef]

81. Stojanovic, M.; Drumond, A.; Nieto, R.; Gimeno, L. Anomalies in Moisture Supply during the 2003 Drought Event in Europe: A Lagrangian Analysis. *Water* **2018**, *10*, 467. [CrossRef]

82. Goudriaan, J. *Crop Micrometeorology: A Simulation Study*; Wageningen University and Research: Wageningen, The Netherlands, 1977.

83. Moreno, M.; Bertolín, C.; Ortiz, P.; Ortiz, R. Satellite Product to Map Drought and Extreme Precipitation Trend in Andalusia, Spain: A Novel Method to Assess Heritage Landscapes at Risk. *Int. J. Appl. Earth Obs. Geoinf.* **2022**, *110*, 102810. [CrossRef]

84. Garrido-Perez, J.M.; Vicente-Serrano, S.M.; Barriopedro, D.; García-Herrera, R.; Trigo, R.; Beguería, S. Examining the Outstanding Euro-Mediterranean Drought of 2021–2022 and Its Historical Context. *J. Hydrol.* **2024**, *630*, 130653. [CrossRef]

85. Vogt, J.; Erian, W.; Pulwarty, R.; Gordon, M. *GAR Special Report on Drought 2021 (United Nations)*; United Nations: Geneva, Switzerland, 2021; ISBN 9789212320274.

86. Pons, X.; Ninyerola, M. Mapping a Topographic Global Solar Radiation Model Implemented in a GIS and Refined with Ground Data. *Int. J. Climatol.* **2008**, *28*, 1821–1834. [CrossRef]

87. Cristóbal, J.; Poyatos, R.; Ninyerola, M.; Llorens, P.; Pons, X. Combining Remote Sensing and GIS Climate Modelling to Estimate Daily Forest Evapotranspiration in a Mediterranean Mountain Area. *Hydrol. Earth Syst. Sci.* **2011**, *15*, 1563–1575. [CrossRef]

88. Cristóbal, J.; Anderson, M.C. Validation of a Meteosat Second Generation Solar Radiation Dataset over the Northeastern Iberian Peninsula. *Hydrol. Earth Syst. Sci.* **2013**, *17*, 163–175. [CrossRef]

89. Gómez-Giráldez, P.J.; Cristóbal Rosselló, J.; Nieto, H.; Diaz-Delgado, R. Estimation of Surface Energy and CO2 Fluxes through Remote Sensing in a Juniper Tree Ecosystem at the National Park of Doñana. In *Proceedings of the RAQRS—VI Recent Advances in Quantitative Remote Sensing, Torrent, Spain, 19–23 September 2022*; Sobrino, J.A., Ed.; RAQRS: Valencia, Spain, 2022; pp. 34–38.

90. Weil, J.C.; Massman, W.J. Lagrangian Stochastic Modeling of Scalar Transport within and above Plant Canopies. In Proceedings of the 22nd Conference on Agricultural and Forest Meteorology, Atlanta, GA, USA, 28 January–2 February 1996; pp. J53–J57.

91. Massman, W.J. A Model Study of KBH^{-1} for Vegetated Surfaces Using 'Localized near-Field' Lagrangian Theory. *J. Hydrol.* **1999**, *223*, 27–43. [CrossRef]